On the physical mechanisms driving the different deep penetration of radiation belt electrons and protons

Journal of Geophysical Research: Space physics

Yang Mei[1,2], Xinlin Li[1,2], Hong Zhao[3], Zheng Xiang[1], Benjamin Hogan[1,2], Declan O'Brien[1,2], and Theodore Sarris[4]

[1]Laboratory for Atmospheric and Space Physics, University of Colorado, Boulder, CO, USA

[2]Department of Aerospace Engineering Sciences, University of Colorado Boulder, Boulder, CO, USA

[3]Department of Physics, Auburn University, Auburn, AL, USA

[4]Department of Electrical and Computer Engineering, Democritus University of Thrace, Xanthi, Greece

Key points:

1. A bi-particle model is established for simultaneously modeling both electron and proton energy-dependent deep penetration to low *L* (<4).
2. Relativistic effect leads to stronger diffusive and convective radial transport of electrons than protons of the same energy.
3. Scattering due to EMIC waves can prevent penetration of 100s of keV protons to low *L* while likely not affecting electrons of the same energy.

Abstract

During active geomagnetic periods both electrons and protons in the outer radiation belt have been frequently observed to penetrate to low *L* (<4). Previous studies have demonstrated systematic differences in the deep penetration of the two species of particles, most notably that the penetration of protons is observed less frequently than for electrons of the same energies. A recent study by Mei et al. (2023, https://doi.org/10.1029/2022GL101921) showed that the time-varying convection electric field contributes to the deeper penetration of low-energy electrons and that a radial diffusion-convection model can be used to reproduce the storm-time penetration of lower-energy electrons to lower *L*. In this study, we analyze and provide physical explanations for the different behaviors of electrons and protons in terms of their penetration depth to low *L*. A radial diffusion-convection model is applied for the two species with coefficients that are adjusted according to the mass-dependent relativistic effects on electron and proton drift velocity, and the different loss mechanisms included for each species. EMIC wave scattering losses for 100s of keV protons during a specific event are modeled and quantified; the results suggest that EMIC waves interacting with protons of lower energies than electrons can contribute to prevent the inward transport of the protons.

1. Introduction

Earth's radiation belts are two donut-shaped regions surrounding Earth where energetic charged particles are trapped by the magnetic field. The outer belt, centered at *L* ~4 (*L* represents the radial distance in Earth radii where the dipole magnetic field line crosses the equatorial plane), normally consists of 10s of keV to several MeV electrons, while the inner belt, centered near L~1.5, is made of 10s – 100s of keV, sometimes up to MeV, electrons and multiple MeV to GeV protons. In between the two belts is the slot region, normally devoid of energetic electrons.

During active geomagnetic periods, outer belt electrons become more dynamic and may penetrate to lower *L* to refill the slot region. Previous studies have shown that such frequently observed inward transport of outer belt electrons is closely associated with plasmasphere reduction or erosion (e.g., Baker et al., 2004; Califf et al., 2017, 2022; Khoo et al., 2018, 2021; Li et al., 2006; Zhao & Li, 2013). In particular, lower energy electrons tend to penetrate to lower *L* more frequently than higher energy electrons (e.g., Reeves et al., 2016). These observations suggest that an energy-dependent mechanism is responsible for the inward transport of lower energy electrons more efficiently. The characteristics of the electron deep penetration phenomenon also include frequent occurrence and relatively rapid time response (e.g., Turner et al., 2017; Zhao et al., 2023). Therefore, the non-diffusive radial transport due to electrostatic large-scale electric fields are believed to be a potential mechanism (Califf et al., 2017; Zhao et al., 2017). To quantify the inward transport of electrons due to storm-time enhanced large-scale electric fields, Mei et al. (2023) added an energy-dependent convection term to the classic radial diffusion model and used this model to study an electron deep penetration event of June 2015. Such inward transport is shown to be most effective for 10s to 100s of keV electrons, whose effect gradually becomes weaker as energy increases, and eventually becomes negligible for > 1 MeV electrons.

Zhao et al. (2023) studied the penetration of energetic electrons and protons to $L<4$ statistically and showed that there are systematic differences between the deep penetration of electrons and protons. More specifically they showed that, while the general trend that lower energy particles can more readily penetrate inward to lower *L* still holds true for protons, electrons penetrate to $L<4$ more deeply, more frequently, and more quickly than protons. While the drift direction of electrons and protons are different, both species should experience the same large-scale electric field as they are drifting around Earth. Motivated by the statistical results of Zhao et al. (2023), we aim to further investigate whether the radial diffusion-convection model can be used to describe simultaneously the behavior of both electron and proton populations, while accounting for the systematic differences as listed above. In particular, this study focuses on investigating the physical mechanisms responsible for the different penetration depths of electrons and protons.

Numerous studies have suggested that injection and radial diffusion are the two major transport and acceleration mechanisms of 10s to 100s of keV protons in near-Earth space (e.g., Gkioulidou et al., 2014, 2015, 2016; Lyu & Tu, 2022; Sheldon & Hamilton, 1993; Zhao et al., 2015). By analyzing long-term proton pressure evolution, Gkioulidou et al. (2016) concluded that injection is the dominant transport and acceleration mechanism for lower energy (<80 keV) protons, while radial diffusion plays a more important role for higher energy (>100 keV) protons. On the other hand, charge exchange and Coulomb scattering are regarded as two major loss mechanisms for protons. Charge exchange is normally seen as the dominant loss mechanism over a wide energy range for ring current protons (Fok et al., 1991; Hamilton et al., 1988; Keika et al., 2006; Kistler et al., 1989). In this study, we consider the charge exchange as one loss mechanism that is continuously active for protons.

Electromagnetic ion cyclotron (EMIC) waves can interact with electrons and protons, causing rapid pitch angle scattering (Summers et al., 2007). Multi-MeV electrons that satisfy resonance conditions can also be scattered by EMIC waves leading to rapid local loss and “bite-out” features (Baker et al., 2021; Engebretson et al., 2018; Ni et al., 2023; Qin et al., 2019; Shprits et al., 2016, 2017; Xiang et al., 2017). Previous studies analyzed and modeled that EMIC waves during geomagnetic storms can lead to precipitation of tens to hundreds of keV protons (Jordanova et al., 2001, 2008; Lyu et al., 2022; Usanova et al., 2010). In this study, we compute the proton lifetime due to EMIC wave scattering for a specific storm event, during which EMIC wave activity has been observed, as reported by Hogan et al. (2023). Proton lifetimes are estimated by a pure pitch angle diffusion simulation based on observed wave properties, and are then implemented as a loss term to the radial diffusion-convection model in addition to other transport and loss mechanisms.

The results point to the following explanations regarding the systematic difference between electron and proton penetration to low *L*: 1. The relativistic effect is less significant for protons than for electrons of the same μ (magnetic moment or the first adiabatic invariant), which leads to weaker radial transport of the protons in both the diffusive and the convective transport mechanisms. The weaker radial transports of protons result in the smaller penetration depth for protons than for electrons. 2. EMIC waves can potentially scatter 100s of keV protons rapidly and prevent their inward transport to a lower *L* than where the local scattering loss happens, while they do not affect electrons of the same energies.

2. Data and Observations

In this study, we use electron differential flux data from the Magnetic Electron Ion Spectrometer (MagEIS) instrument (Blake et al., 2013) and proton differential flux data from the Radiation Belt Storm Probes Ion Composition Experiment (RBSPICE) instrument (Mitchell et al., 2013) onboard the Van Allen Probes (also known as Radiation Belt Storm Probes, or RBSP) (Mauk et al., 2013). Both particle instruments provide pitch angle resolved particle fluxes.

Two geomagnetic storm events are selected as case studies to quantitatively investigate the differences in the penetration depth of electrons and protons: the first event is a storm with minimum Dst=-67 nT that occurred on June 8, 2015, whereas the second event is a storm with minimum Dst=-44 nT that occurred on November 4, 2014. Figures 1 and 2 present the particle flux observations for the two events, respectively, at selected energies from ~80 to 500 keV combining RBSP A&B data as a function of time and *L* before, during, and after the two storms. Electron fluxes are shown on the left-hand side and proton fluxes are on the right. The central energy of each electron channel is given in the upper left corner of each panel. It is noted that for electrons the central energy is slightly different between RBSP A and B. It is also noted that the electron and proton energy channels from the MagEIS and RBSPICE instruments do not exactly overlap; we thus choose to display the energy channels with the closest corresponding energy ranges. The color scale showing the flux levels is the same for both the electron and proton energy channels. The Dst index, provided by the WDC for Geomagnetism Kyoto, is plotted on the bottom (http://wdc.kugi.kyoto-u.ac.jp/wdc/Sec3.html). For electrons, all four energy channels show a similar trend, with fluxes that are largely enhanced during the storm main phase and remain elevated after the storm. Electron fluxes at lower energies increased faster and extended to lower *L* than those at higher energies. While the pre-storm electron fluxes in the outer belt for Event 1 were at a lower level than Event 2, the enhanced fluxes looked similar at the end of the selected period for both events. For protons, only the 82 keV channel shows a clear flux enhancement at $L>\sim3.5$ for the two events. There is no enhancement of higher energy proton fluxes at $L<4$, while fluxes at $L>4$ slightly decreased or remained the same as the pre-storm levels. Thus, as shown in Figures 1 and 2, electrons and protons of the same energies respond very differently during both storms.

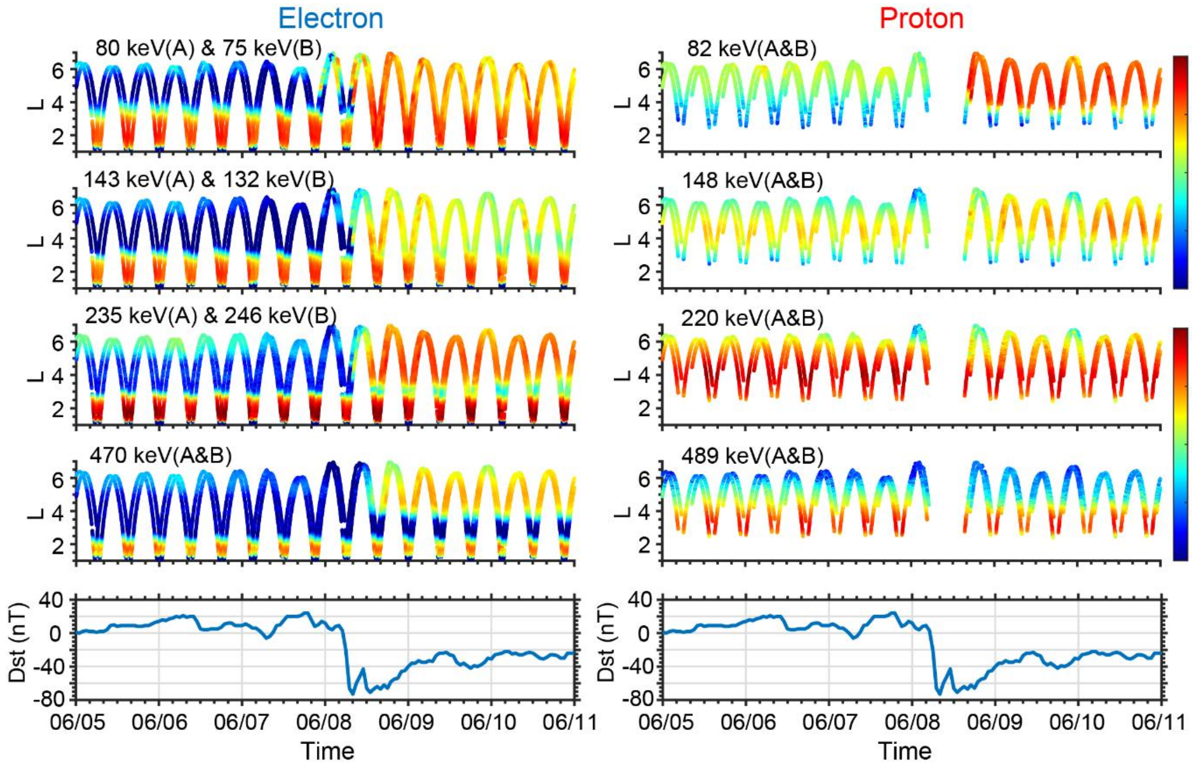

Figure 1. Electron and proton flux measurements by RBSP A & B during a geomagnetic storm on June 8, 2015. (left) Electron fluxes measured by the MagEIS instrument at selected energies as a function of time and L. (right) Proton fluxes measured by the RBSPICE instrument at similar energies in the same format. Dst index is provided by Kyoto University.

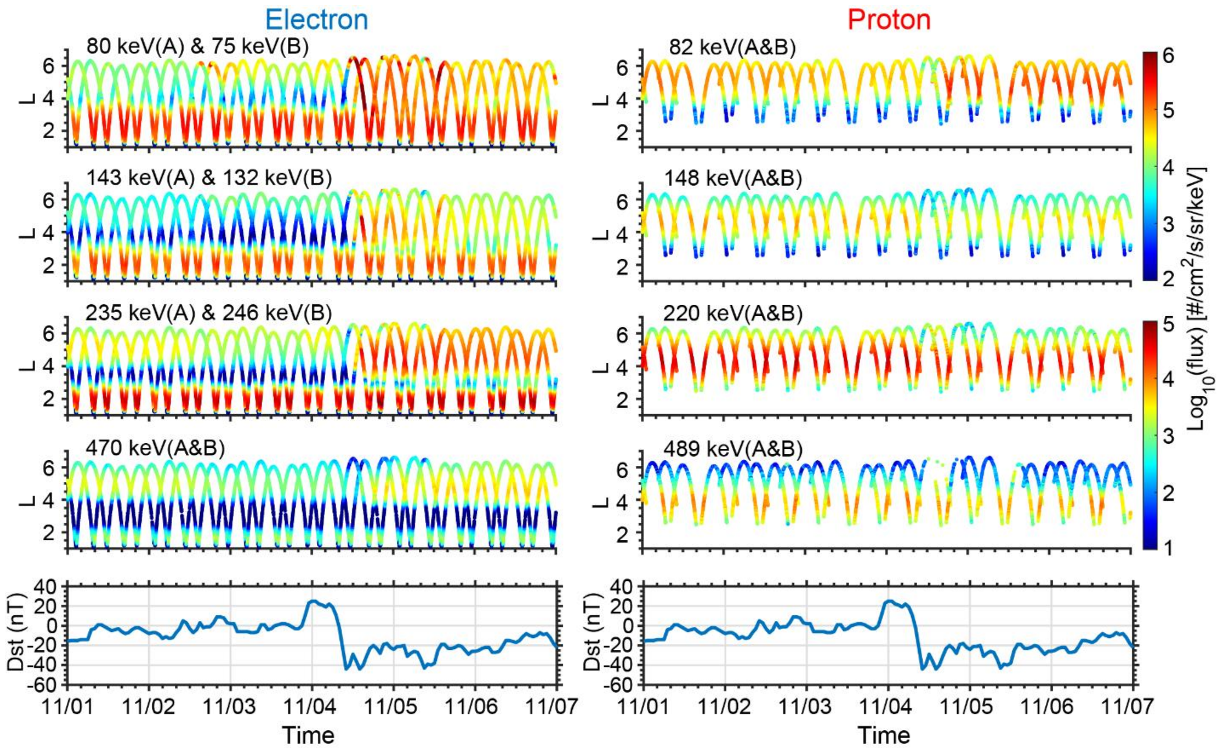

Figure 2. Electron and proton flux measurements by RBSP A & B in the same format as Figure 1 during a geomagnetic storm on November 4, 2014.

In order to better understand the mechanisms that govern particle dynamics and the different behavior to the two particle species, in the following we further investigate the two events by simulating the evolution of phase space density (PSD) of the two species. We convert both electron and proton differential fluxes $j_s(E_i, \alpha, L)$ to PSD $f_s(\mu, K, L^*)$ using flux data from RBSP A&B based on the relation $f_s(\mu, K, L^*) = \frac{j_s(E_i,\alpha,L)}{P^2}$, where *f* is the PSD of the trapped particles, *P* is the particle momentum, E_i is the particle energy, α is the pitch angle, subscript *s* represents the particle species (*p* for protons or *e* for electrons), *L* is the McIlwain *L*, $\mu = \frac{P_\perp^2}{2m_0B}$, $K = \int_{s_m}^{s_m'} \sqrt{B_m - B(s)}ds$, L^* is the Roederer *L*: $L^* = \frac{2\pi M}{|\Phi| R_E}$ (Roederer, 1970), where Φ is the third adiabatic invariant and *M* is the Earth's dipole magnetic moment. *K* and L^* are calculated based on the TS04 model (Tsyganenko & Sitnov, 2005) provided by the Van Allen Probes Magnetic Ephemeris files (Spence et al., 2013); μ is calculated using the local magnetic field strength. For this study, we focus on near-equatorial particles, therefore a relatively small *K* value, $K = 0.12\ G^{1/2}R_E$, is selected for both electron and proton PSD. Since the PSD depends on the rest mass of particles, the electron PSD will be orders of magnitude greater than proton PSD for similar flux values of the two species.

3. Methodology and Model Description

Based on the energy-dependent radial diffusion-convection model by Mei et al. (2023), we further developed a bi-particle model for electrons and protons:

$$\frac{\partial f_s}{\partial t} = L^{*2}\frac{\partial}{\partial L^*}\left[\frac{D_{L^*L^*,s}}{L^{*2}}\frac{\partial f_s}{\partial L^*}\right] + V_{R,s}(R,t)\frac{\partial f_s}{\partial R} + S_s - \frac{f_s}{\tau_s} \tag{1}$$

where, further to the variables defined above, R is the radial distance in Earth's radii, $D_{L^*L^*}$ is the radial diffusion coefficient, $V_{R,s}$ is the convection coefficient representing the transport due to time-variant large-scale electric fields, S_s is the source rate for each species due to local heating or injection, and τ_s is the particle lifetime for each species. This 1-D diffusion-convection model is then used to quantify the radial transport of trapped particles due to enhanced large-scale electric fields by assuming: 1. a dipole magnetic field configuration, 2. a symmetric large-scale electric field which linearly changes within a 1-hr interval, 3. the presence of outward radial gradients in PSD.

The PSD radial profile derived from flux measurements before the storm is used as an initial condition for the model. The observed PSD at the highest available L^* is regarded as the outer boundary condition throughout the model. Relatively small values of PSD, 1×10^{-8} $(c/MeV/cm)^3$ for electrons and 1×10^{-10} $(c/MeV/cm)^3$ for protons are respectively set as the inner boundary condition at L^*=1.1 for the two species. For the two moderate storm events that are simulated in this study local heating effects are not considered. The source term S_s is set to 0 in the model, while part of the local heating or injection effects might be implicitly implemented to the model as the observed PSD at the highest available L^* is used as the outer boundary condition.

In the rest of this section, we discuss in further detail the various parameters of the model, namely the radial diffusion coefficient, the time-varying electric field model, the electron loss term and the proton loss terms.

3.1 Radial diffusion

A μ-dependent empirical radial diffusion coefficient model $D_{LL,Liu}$ (Liu et al., 2016) has been extended to low μ (10-400 MeV/G) as a modified radial diffusion coefficient, $D_{LL,Liu-mod}$ for electrons (Mei et al., 2023). Based on $D_{LL,Liu-mod}$ for electrons, we analyze the difference between electron and proton drift periods to estimate the corresponding radial diffusion coefficients for protons, by assuming that the ULF waves are symmetrically distributed and propagating in the azimuthal coordinate during the storm. Under this assumption, electrons and protons will interact accordingly with the ULF waves of the same power spectrum, and radial diffusion coefficient will be the same for electrons and protons of the same drift frequency.

Due to the lower mass of electrons, they will be affected more significantly by the relativistic effect than protons of the same kinetic energy, thus drifting slower than the protons. A bounce-averaged relativistic drift period formula in dipole field is given by (Schulz & Lanzerotti, 1974):

$$\tau_D = \frac{2\pi|q|B_0R_E^2}{3m_0c^2\gamma\beta^2L}\frac{T(\alpha_e)}{D(\alpha_e)} \tag{2}$$

where m_0 is the rest mass of the trapped particle, $B_0 = 31000\,nT$ is the equatorial magnetic field strength at the Earth's surface, $R_E = 6370\,km$ is the Earth's radius, q is particle charge, γ is the Lorentz factor, β is the ratio of particle velocity to the speed of light, and T and D are pitch angle-dependent functions.

As an illustration, Figure 3 shows the difference between electron and proton drift speeds at L=3 and L=4. The left column of Figure 3 compares their drift velocities as a function of energy. The drift velocity of a 1 MeV electron is about 30% slower than a 1 MeV proton. The middle column of Figure 3 shows the ratio between the electron and proton drift period at the same μ for L=3 and L=4. Converting to the μ coordinate, we can see that the background magnetic field strength plays a role and thus the drift difference of the two species becomes L-dependent. The value of $\frac{\tau_{D,e}}{\tau_{D,p}}$ increases to 1.7 for L=4 and to 2.35 for L=3 when μ increases to 100 MeV/G (corresponds to ~0.36 MeV at L=4 in dipole field). As electrons and protons are transported inward to lower L the drift period difference increases. In addition, we show the relation between the μ of electron and proton that result in the same drift period in the right column of Figure 3. Based on equation (2), electrons and protons of the same drift period should obey the following equation:

$$\frac{\mu_e^2 E_{0,e}}{2\mu_e B(L) + E_{0,e}} = \frac{\mu_p^2 E_{0,p}}{2\mu_p B(L) + E_{0,p}} \tag{3}$$

where $E_{0,e}$ and $E_{0,p}$ are, respectively, the rest energy of an electron and a proton, and μ_e and μ_p are the corresponding magnetic moments of an electron and a proton with the same drift period. The right column of Figure 3 shows the correspondence of μ_e and μ_p at different L. At L=4 an electron of μ=100 MeV/G approximately has the same drift period as a 60 MeV/G proton, while this drift-period alignment shifts to μ ~42 MeV/G protons at L=3.

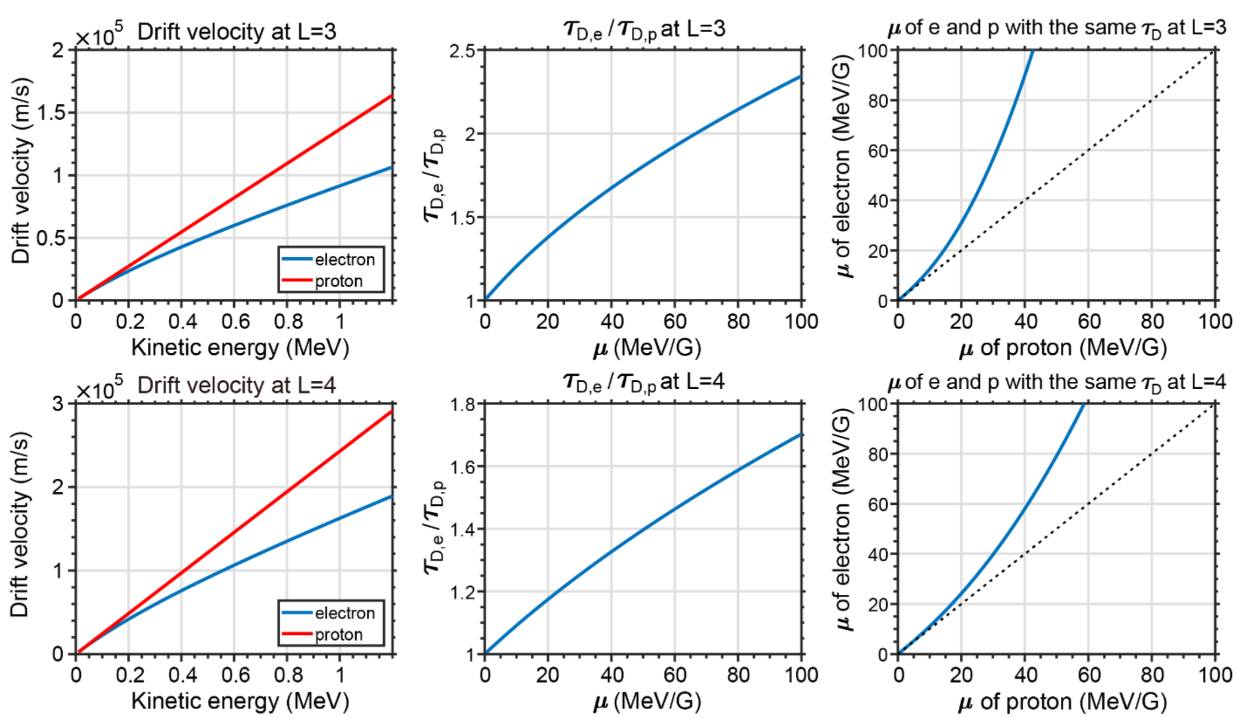

Figure 3. The drift differences between electrons and protons at L=3 (top panels) and L=4 (bottom panels). (left) Drift velocities of electrons and protons as a function of kinetic energy. (middle) The ratio between electron and proton drift period as a function of μ. (right) Correspondence of electron and proton magnetic moment μ with the same drift period.

For electrons, the $D_{LL,Liu-mod}$ is used as the radial diffusion coefficient (Mei et al., 2023):

$$D_{L^*L^*,e} = D_{LL,Liu-mod} = 1.115 \cdot 10^{-6} \cdot 10^{a \times K_p + b} \cdot L^{8.184} \cdot \mu^c \cdot d$$
$$a = 0.35;\ b = -0.414;$$
$$c = -0.57;\ d = 0.796 \qquad (4)$$

For protons, a corresponding radial diffusion coefficient according to our assumptions of the ULF perturbations can be expressed as:

$$D_{L^*L^*,p}(\mu) = D_{L^*L^*,e}(\mu') = 1.115 \cdot 10^{-6} \cdot 10^{a \times K_p + b} \cdot L^{8.184} \cdot \mu'^{c} \cdot d \qquad (5)$$

where the μ' meets the condition $\tau_{D,e}(\mu') = \tau_{D,p}(\mu)$. The value of μ' is given by the positive root of a polynomial equation: $E_{0,e}\mu'^2 - \frac{2B(L)\mu^2 E_{0,p}}{2\mu \cdot B(L) + E_{0,p}}\mu' - \frac{\mu^2 E_{0,p} E_{0,e}}{2\mu \cdot B(L) + E_{0,p}} = 0$.

3.2 Time-varying electric field induced convection

The energy-dependent convection coefficient $V_{R,s}$ follows the same formulation as the one introduced by (Mei et al., 2023):

$$V_{R,s}(R,t) = \left|\frac{\boldsymbol{E}_{net,s} \times \boldsymbol{B}}{B^2}\right| \qquad (6)$$

with

$$\boldsymbol{E}_{net,s} = \frac{\int_{\frac{\pi}{2}}^{\frac{3\pi}{2}} E_\phi(R,\phi,t)d\phi}{\pi} \cdot \frac{\tau_{D,s}}{4\tau_E}$$

where $\boldsymbol{B}$ is the magnetic field strength, E_ϕ is the azimuthal component of the large-scale electric field, which in this case is the modified Volland-Stern model based on Mei et al. (2023), R is the radial distance, ϕ is the azimuthal angle, $\tau_{D,s}$ is the particle drift period, and τ_E is the characteristic timescale of the electric field time-variation: $\tau_E(R,t) = \frac{\int_{\frac{\pi}{2}}^{\frac{3\pi}{2}} E_\phi(R,\phi,t)d\phi}{\left|\frac{\partial \int_{\frac{\pi}{2}}^{\frac{3\pi}{2}} E_\phi(R,\phi,t)d\phi}{\partial t}\right|}$.

Since the coefficient $V_{R,s}$ is proportional to the particle drift period $\tau_{D,s}$, the drift period difference of the same μ electron and proton shown in Figure 3 will result in different strength on the convective transport. As discussed before, the ratio of $\frac{\tau_{D,e}}{\tau_{D,p}}$ increases more significantly at lower L, which suggests that for electrons and protons of the same μ, the convection coefficient for proton will decrease faster than that of electron as they are being transported inward to lower L.

3.3 Electron loss

The dominant loss mechanism for 10s to 100s of keV electrons is pitch angle scattering due to interactions with plasma waves including chorus and plasmaspheric hiss. In this study, we use empirical models of electron lifetime due to the chorus and hiss wave scattering (Orlova & Shprits, 2014; Zhu et al., 2021). Using realistic chorus wave parameters, Orlova and Shprits (2014) established a parameterized electron lifetime model as a function of geomagnetic activity, electron energy, and locations. Specifically, in their model, lifetimes for 1 keV-2 MeV electrons can be calculated in four MLT sectors, including the night, dawn, prenoon, and postnoon, can be calculated with a given Kp index and radial distance R. Zhu et al. (2021) developed an empirical model for the lifetime of slot region electrons due to plasmaspheric hiss waves using a statistically averaged spectrum of RBSP observations. The energy range of the model is from 0.01 to 10 MeV, and model inputs include L and the AE index.

We use the electron lifetime model τ_{chorus} by Orlova and Shprits (2014) outside the plasmapause to account for chorus wave scattering loss and the electron lifetime model τ_{hiss} by Zhu et al. (2021) inside the plasmapause to quantify hiss wave scattering loss. The overall electron lifetime can be written as:

$$\tau_{electron} = \begin{cases} \tau_{chorus}, L > L_{PP} \\ \tau_{hiss}, L < L_{PP} \end{cases} \quad (7)$$

where L_{PP} is the L of the plasmapause location, which is considered here as a boundary separating the two types of electron losses. L_{PP} is calculated herein based on the Carpenter and Anderson (1992) empirical model. Since the diffusion-convection model we use in this study is dependent only on the radial distance, and not on MLT, we use the minimum electron lifetime among four MLT sectors as calculated by the Orlova & Shprits (2014) model to represent the drift-averaged lifetime for electrons, considering that the drift periods of outer belt electrons at 100s of keV are ~ 1 hour while their lifetimes are several hours to days. It is noted that the empirical model of Zhu et al. (2021) for electron loss timescales due to plasmaspheric hiss wave scattering is applicable in the range $1.8<L<3$, while the plasmapause location is sometimes higher than $L=3$, as, for example, during geomagnetically quiet times before a storm. In such cases, we interpolate the electron loss timescale in the logarithmic scale when there is a gap in the τ_{hiss} model between $L=3$ and L_{PP} during quiet time.

3.4 Proton loss

Charge exchange and EMIC wave scattering are the two main loss mechanisms considered in this study. Unlike the almost ubiquitous loss mechanism of charge exchange which protons are continuously undergoing, EMIC wave scattering loss largely depends on the spatial presence, magnitude, and frequency range of EMIC waves, which differ from case to case. Thus, the computation of loss timescale is nontrivial due to limited spatial and temporal coverage of the wave measurements. For this study, we only compute the proton loss due to EMIC wave scattering for Event 1, the June 8 storm in 2015, during which He+ band EMIC wave activities have been observed and studied by Hogan et al. (2023), to elaborate the contribution of EMIC wave to the deep penetration difference.

Charge exchange loss:

A bounce-averaged lifetime expression by Smith et al. (1976) is used to obtain the charge exchange lifetime for protons:

$$\tau_{CE} = \tau_{eq} \cos^{3.5\pm0.2} \lambda_m \tag{8}$$

with

$$\tau_{eq} = \frac{1}{\sigma n v}$$

where τ_{eq} is the estimated mean lifetime of protons evaluated at the equatorial plane (Smith & Bewtra, 1978), λ_m is the mirror latitude, σ is the charge exchange cross section, n is the number density of neutral atoms, and v is the velocity of the incident particle. The charge exchange cross section σ depends on energy and on the type of charge transfer process. We use the parameterized cross sections as a function of energy as provided by Lindsay and Stebbings (2005). The experimentally determined relation between hydrogen atom energy and cross-section area applies for <250 keV protons. We extrapolate the relation for higher energy. We use the exospheric density model by Chamberlain (1963) to estimate the neutral density in the inner magnetosphere:

$$n(r) = N_c e^{-(\lambda_c - \lambda(r))} \zeta(\lambda) \tag{9}$$

where λ represents the potential energy: $\lambda(r) = \frac{G\mu_E M}{kT_c r}$, G is the gravitational constant, μ_E is the planetary mass (Earth's mass in this case), M is the atomic mass, k is the Boltzmann constant, r is radial distance, and N_c and T_c are respectively the neutral density and temperature at the exobase which is assumed to be at 500 km, ζ is a partition function. Knowing that the charge exchange lifetime depends on the neutral atom species, we compared two main types of charge exchange in Earth's magnetosphere, H^+-H and H^+-O, with typical exospheric neutral hydrogen and oxygen densities. Our results show that the lifetime due to H^+-H interaction is orders of magnitude shorter than that of H^+-O type interaction (shown in Supporting Information Figure S1). Therefore, we use the bounce-averaged lifetime of proton charge exchange with neutral hydrogen as the dominant charge exchange loss mechanism for protons. The top of Figure 4 shows the charge exchange lifetime of proton interacting with neutral hydrogen atoms as a function of radial distance and μ, assuming that $N_c = 4 \times 10^4\ \#/cm^3$ and $T_c = 1000\ K$. We can see that typically the lifetime is shorter for the same μ protons at distances farther away from Earth.

During storm times, the two primary parameters determining proton lifetime, namely neutral hydrogen density and temperature in the exosphere, may experience dynamic changes. To quantify the influence of exospheric variations, we use the NRLMSIS 2.0 model (Emmert et al., 2021) to obtain neutral hydrogen density and exospheric temperature at 500 km height for the two selected storms. Since the exospheric density model by Chamberlain (1963) follows the assumption of spherical symmetry, we averaged the hydrogen density and exospheric temperature at different local times to obtain N_c and T_c for the selected events, which are presented at the bottom of Figure 4 (see Figures S2 & S3 in Supporting Information for details).

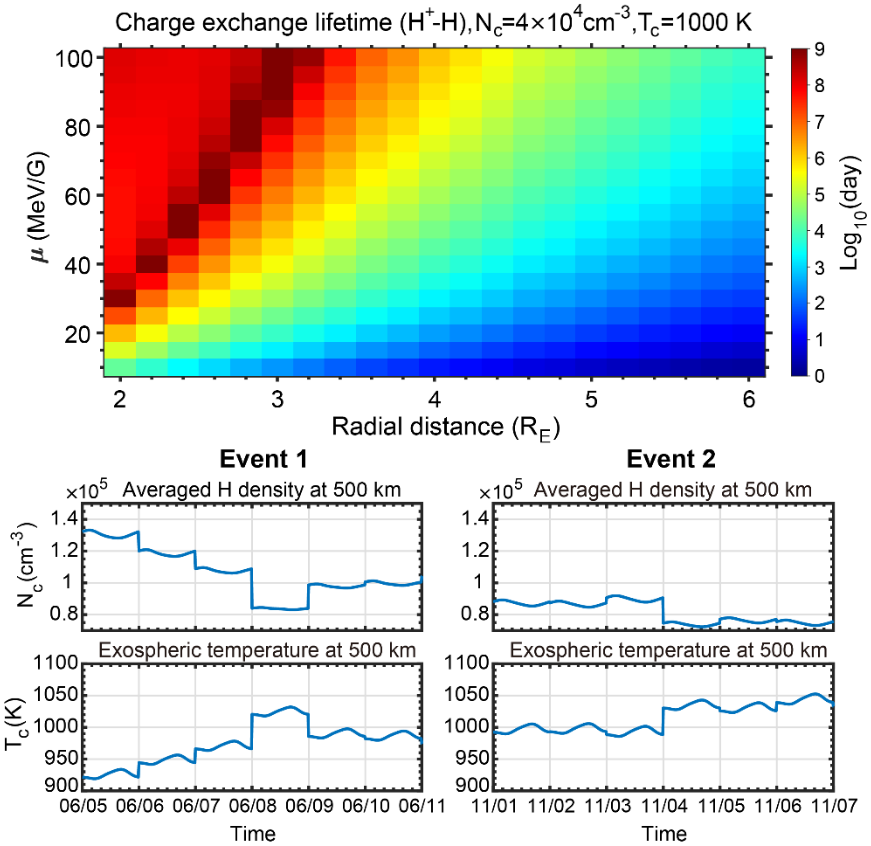

Figure 4. (top) Charge exchange lifetime for protons due to H^+-H interaction as a function of radial distance and magnetic moment μ assuming fixed density and exospheric temperature at 500 km exobase. (bottom) Averaged hydrogen density and exospheric temperature over longitudes and latitudes at 500 km during the two selected events provided by the NRLMSIS 2.0 model (Emmert et al., 2021).

EMIC wave scattering loss (only applied to Event 1):

As shown in Figure 3 of Hogan et al. (2023), He+ band EMIC wave signatures were observed by RBSP near L^*=4.1 to 4.3 around 4:45 UT on 8 June 2015. The frequency range of the observed EMIC wave signatures is ~1.29f_{O+} to ~1.77f_{O+}, where f_{O+} represents the local oxygen gyrofrequency.

The proton lifetime in the presence of EMIC wave scattering can be estimated by conducting a 1-D pitch angle diffusion simulation (Meredith et al., 2006; Ni et al., 2015; Thorne et al., 2013):

$$\frac{\partial f_p}{\partial t} = \frac{1}{T(\alpha_{eq})\sin(2\alpha_{eq})}\frac{\partial}{\partial \alpha_{eq}}\left[T(\alpha_{eq})\sin(2\alpha_{eq})\langle D_{\alpha\alpha}\rangle\frac{\partial f_p}{\partial \alpha_{eq}}\right] \tag{10}$$

where α_{eq} is the equivalent equatorial pitch angle, $<D_{\alpha\alpha}>$ is the bounce-averaged pitch angle diffusion coefficient, $T(\alpha_{eq})$ is the bounce period approximated by: $T(\alpha_{eq}) = 1.3802 - 0.3198\left[\sin(\alpha_{eq}) + \sqrt{\sin(\alpha_{eq})}\right]$ (Lenchek et al., 1961).

The bounce-averaged pitch angle diffusion coefficient $<D_{\alpha\alpha}>$ is computed using the full diffusion code (Ni et al., 2011; Ni et al., 2008; Shprits & Ni, 2009) at L=4.1, 4.2, and 4.3, based on assumptions of cold plasma and dipole magnetic field. We use the density model by Sheeley et al. (2001): $N_0 = 1390\,(3/L)^{4.83}\ cm^{-3}$ for determining the electron density at the selected L. A Gaussian fit is used to provide the power spectra of the EMIC wave. The local plasma composition is assumed to be 94% H+, 5% He+, and 1% O+ as found by Kersten et al. (2014). Top left of Figure 5 shows $<D_{\alpha\alpha}>$ for proton computed at L=4.2. The $<D_{\alpha\alpha}>$ for proton at L=4.1 and 4.3 can be found in the Supporting Information Figure S4.

With the calculated $<D_{\alpha\alpha}>$, we conducted pitch angle diffusion simulations based on equation (10) for L=4.1-4.3. The right-column panels of Figure 5 show the three examples of the simulated time variations of proton flux at 136.8, 273.5, and 444.4 keV at L=4.2. The estimation of proton lifetime is taken after reaching equilibrium and will not be affected by the initial distribution. Normalized flat pitch angle distribution of proton fluxes is used as the initial condition. We assume that the EMIC waves with the observed power spectra are evenly distributed over MLT for simplicity. In reality, EMIC waves might be confined in narrower MLT ranges, but waves with stronger wave power can still result in similar scattering effect considering the spatial and temporal uncertainties of observations. The upper boundary condition is set as $\frac{\partial f_p(\alpha_{eq}=90°)}{\partial \alpha_{eq}} = 0$, while the lower boundary condition is set as $f_p(\alpha_{eq} < \alpha_{LC}) = 0$, α_{LC} is the equatorial bounce loss cone given by $\sin(\alpha_{LC}) = [L^5(4L-3)]^{-1/4}$ (Summers et al., 2007), which is around 4.95° at L=4.2 for Event 1. The simulation is conducted for 5000 seconds, and the proton fluxes reach equilibrium before the end of the simulation. From the right column panels of Figure 5, we can see that as the proton energy increases, the resonant region shifts to a higher pitch angle, while diffusion becomes weaker as the $<D_{\alpha\alpha}>$ decreases.

By assuming $\frac{\partial f_p}{\partial t} = -\frac{f_p}{\tau_{EMIC}}$, the lifetime of K=0.12 $G^{1/2}R_E$ protons is estimated by:

$$\tau_{EMIC} = \frac{\Delta t}{\ln\left(\frac{j_p(\alpha_K, t_n)}{j_p(\alpha_K, t_n + \Delta t)}\right)} \tag{11}$$

where j_p is the proton flux converted from proton PSD f_p, α_K is the corresponding pitch angle of K=0.12 $G^{1/2}R_E$ protons, Δt is the time step of the pitch-angle diffusion simulation, and t_n denotes a simulation time stamp after reaching the equilibrium state. At L=4.2, α_K is around 51° for Event 1. For protons outside of the resonant region with EMIC waves, τ_{EMIC} is infinite.

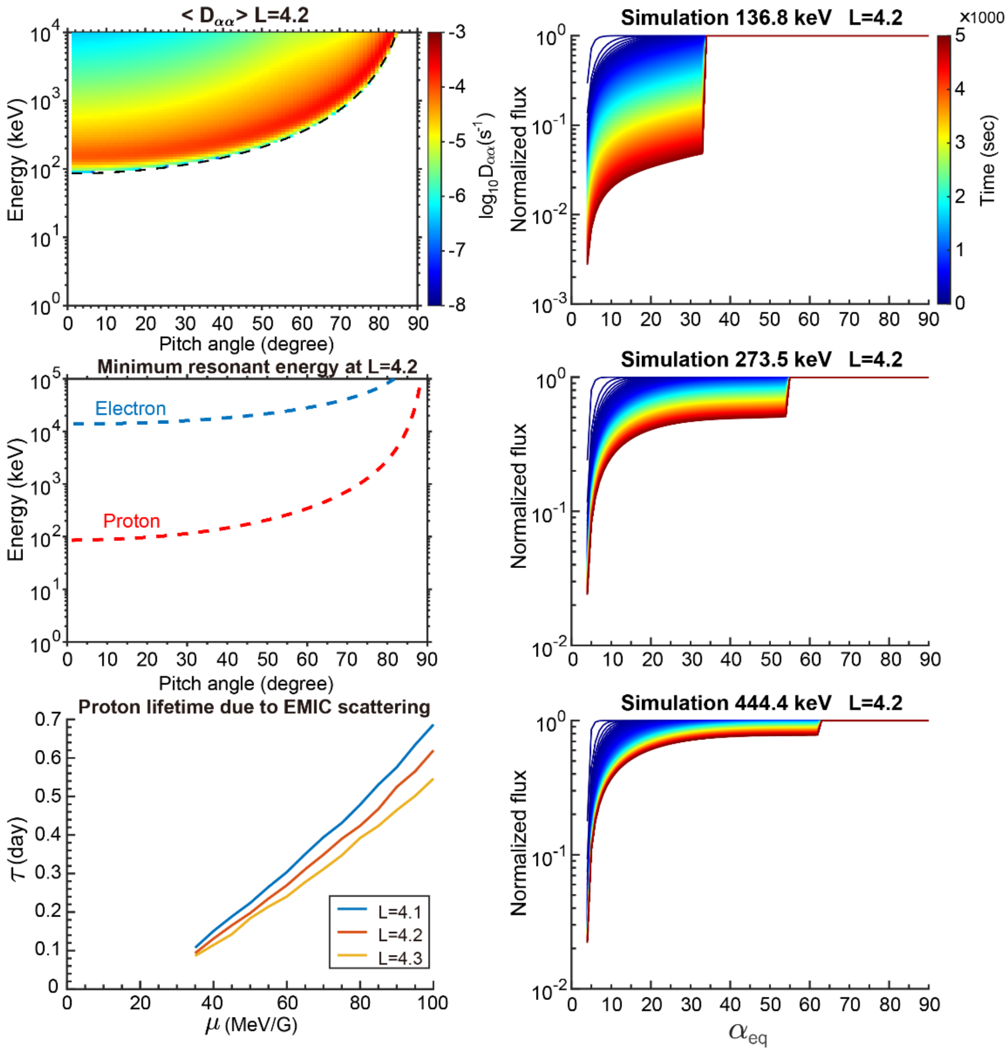

Figure 5. Estimations of proton lifetime due to EMIC wave scattering loss during Event 1 (2015 June 8 storm) based on wave observations of Hogan et al. (2023). (Top left) The bounce-averaged pitch angle diffusion coefficient $\langle D_{\alpha\alpha}\rangle$ at L=4.2; (Middle left) Minimum resonant energy of the EMIC wave with electron (in blue) and proton (in red) at L=4.2; (Right) From top to bottom we show the pitch angle diffusion simulation results of protons at the selected energies at L=4.2; (Bottom left) The estimated proton lifetime at L=4.1, 4.2, and 4.3 as a function of magnetic moment for K=0.12 $G^{1/2}R_E$ protons.

The bottom left panel of Figure 5 shows our estimate of the μ-dependent proton lifetimes considering EMIC wave scattering effects at L=4.1, 4.2, and 4.3 during Event 1. Protons of μ <35 MeV/G are outside of the resonant region for the observed EMIC waves; for >35 MeV/G protons, τ_{EMIC} increases from ~0.1 to >0.5 day as μ increases. The difference between τ_{EMIC} at different Ls is not obvious. Additionally, the middle-left panel of Figure 5 compares the minimum resonant energies of electrons and protons with the observed EMIC waves, showing that the minimum resonant energy for electrons is higher than 10 MeV. Thus, there is no EMIC wave scattering loss for <100 MeV/G electrons that we focus on in this study.

To summarize, the proton lifetime model we use in this study is expressed as:

$$\tau_{proton} = \begin{cases} \min(\tau_{EMIC}, \tau_{CE}), 4.1 \le L \le 4.3 \; for \; Event \; 1 \\ \tau_{CE}, other \end{cases} \quad (12)$$

where the minimum between τ_{EMIC} and τ_{CE} is taken as the proton lifetime for the L range of 4.1 to 4.3 from 04:30 to 19:00 on June 8, 2015. In the absence of EMIC wave effects, only charge exchange loss contributes to the loss of protons.

4. Results

4.1 Event 1 (2015 June 8 storm)

We first present the results of radial diffusion and convection modeling conducted for μ=10-100 MeV/G, K=0.12 $G^{1/2}R_E$ electrons and protons for the 2015 June 8 storm. Figure 6 and Figure 7 respectively compare the observed and modeled results for 20 MeV/G and 50 MeV/G electrons (left) and protons (right). The top row shows the PSD converted from RBSP A & B flux observations. The second row of panels displays the modeled PSD of the bi-particle model. Black dashed curves indicate the empirical plasmapause location (Carpenter & Anderson, 1992). The third to fifth panels respectively present the radial diffusion coefficient D_{LL}, radial convection coefficient V_R, and particle lifetime during the simulated period for electrons and protons. The last four panels at the bottom of Figure 6 display comparisons between observed (blue circle) and simulated (orange curve) 20 MeV/G electron and proton PSD at L=3, 3.5, 4, and 4.5. In Figure 7, comparisons for 50 MeV/G and 0.12 $G^{1/2}R_E$ particle PSD at L=3.5, 4, and 4.5 are shown in the same format.

Overall, the bi-particle model captures the rapid inward penetration feature for both electrons and protons. The radial diffusion coefficient D_{LL} and convection coefficient V_R for electrons and protons significantly enhanced at the storm main phase. The timescale of the loss process is largely different for the two particle species. For low μ (e.g., 20 MeV/G) protons not resonating with the observed EMIC waves, charge exchange dominates their losses. Generally, electron lifetimes are >1 order of magnitude shorter than those of protons without the presence of EMIC waves. Considering EMIC wave scattering loss, proton lifetime can be shortened to the order of hours. The line plots at the bottom of Figures 6 & 7 display detailed different deep penetration of the two particle species reproduced by the model. For 20 MeV/G, a relatively low μ, both species show similar deep penetration characteristics at L=4 & 4.5, in which PSD rapidly enhanced for nearly 2 orders of magnitude. At L=3 & 3.5, the relativistic effects on the radial diffusion and convection of electrons are more significant, resulting stronger radial transport of them. Modeled electron PSD there showed consistently more enhancements than the proton PSD, which matches the observation. When μ increases to 50 MeV/G, the difference between electron and proton deep penetrations enlarges as both the relativistic effect and EMIC wave scattering play significant roles. Across a wide L range from 3.5 to 4.5, while electron PSD largely increased for more than two orders of magnitude, the proton PSD remained at the same level as pre-storm.

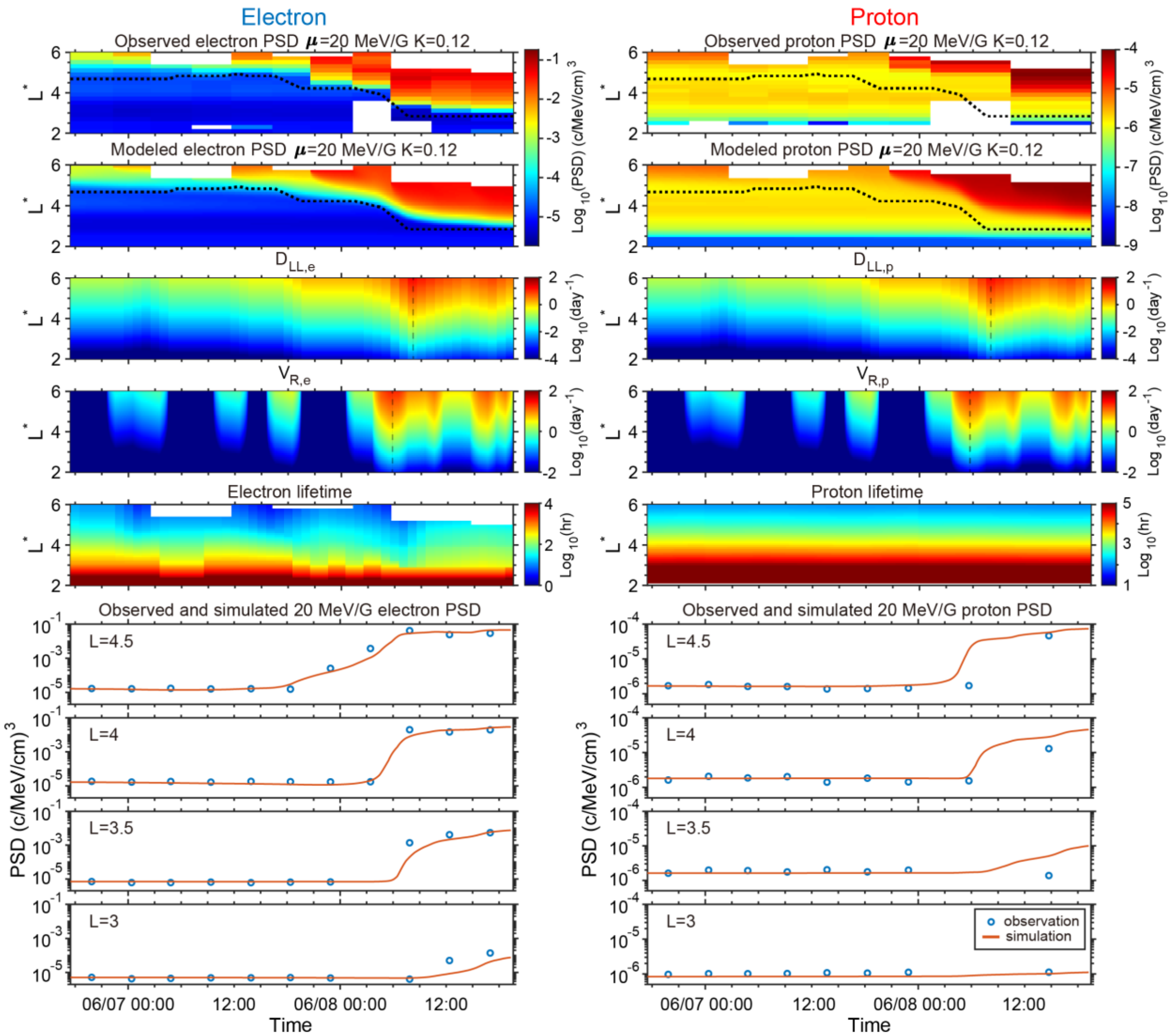

Figure 6. Modeled results for 20 MeV/G electrons (left column) and protons (right column) during Event 1. From top to bottom, we display the observed PSD, modeled PSD, radial diffusion coefficients, convection coefficients, particle lifetime, and comparisons between observation and model at selected L as a function of time.

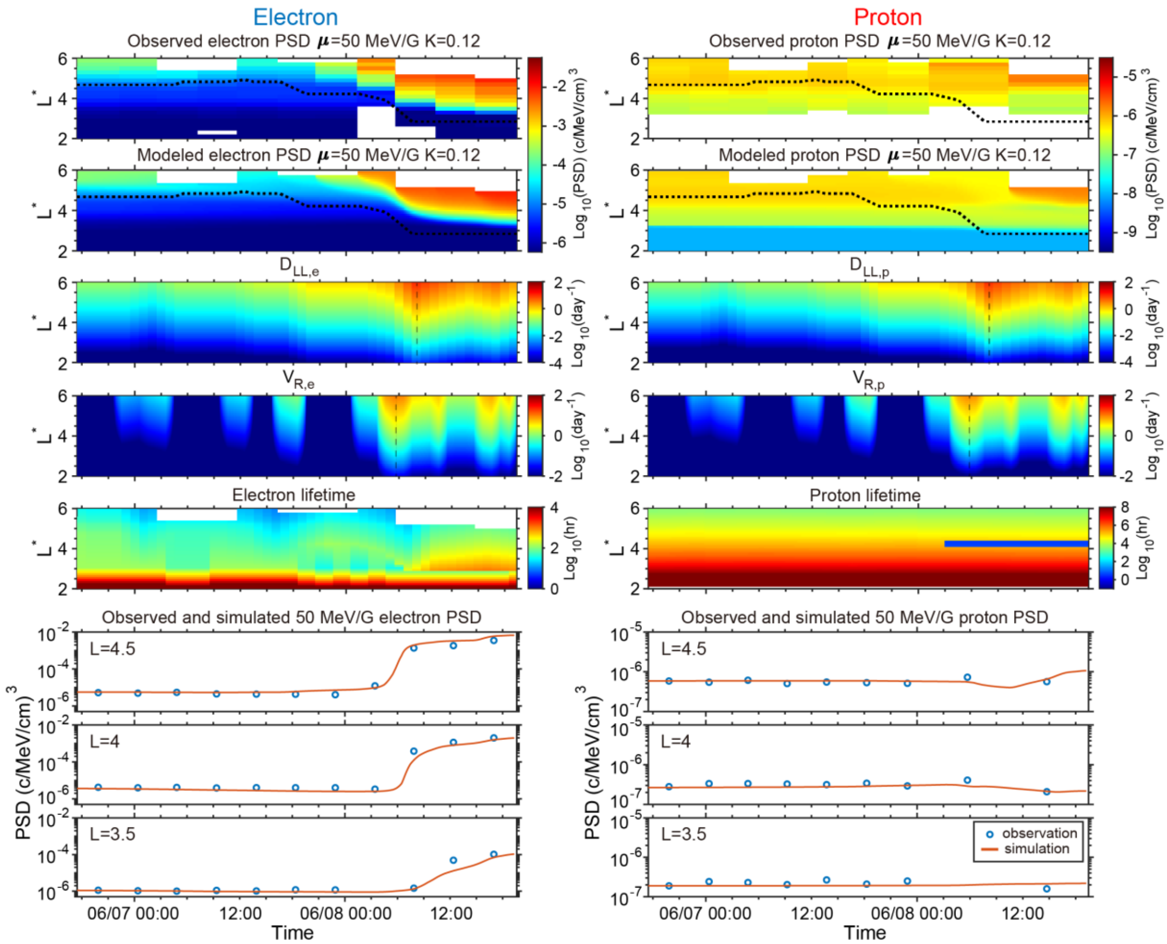

Figure 7. Modeled results for 50 MeV/G electrons (left column) and protons (right column) during Event 1 in the same format as Figure 6.

To quantitatively show the impact of relativistic effect on the radial transport of electrons and protons, we compare the maximum radial diffusion and convection coefficients for the two species during Event 1 in Figure S5. As indicated by the dashed lines in the third and fourth panels of Figure 6, diffusion coefficients D_{LL} reach their maximum values around 07:30 UT, while the convection coefficients V_R peak at around 05:30 UT. In Figure S5, the ratio of the convection coefficient of proton over that of electron, $V_{R,p}/V_{R,e}$, is shown by the left panel, while the ratio of the diffusion coefficient, $D_{LL,p}/D_{LL,e}$, is plotted on the right. The coefficients for 10, 20, and 50 MeV/G are compared and presented as a function of *L*. A general trend for both $D_{LL,p}/D_{LL,e}$ and $V_{R,p}/V_{R,e}$ is that the ratios continuously decrease when moving to lower *L*. For 10 MeV/G, at *L*=5, the ratios of diffusion and convection coefficients are close to 1, which is consistent with the observation that ~80 keV electrons and protons experience flux enhancement at a similar level. As μ increases from 10 to 50 MeV/G, V_R and D_{LL} for protons become significantly smaller than those for electrons at all *L*s. For μ=50 MeV/G, $V_{R,p}$ drops from 80% of $V_{R,e}$ to 35% moving from *L*=5 to 2, while $D_{LL,p}$ is consistently lower, less than 40% of $D_{LL,e}$ across the *L* range from 1.5 to 5. Note that the values of $D_{LL,e}$ and $V_{R,e}$ also experience a dramatic decrease moving to lower *L*. This indicates that as μ increases the radial diffusion and convection processes for protons decrease faster than those for electrons. Thus, protons cannot be radially transported to a low *L* as electrons.

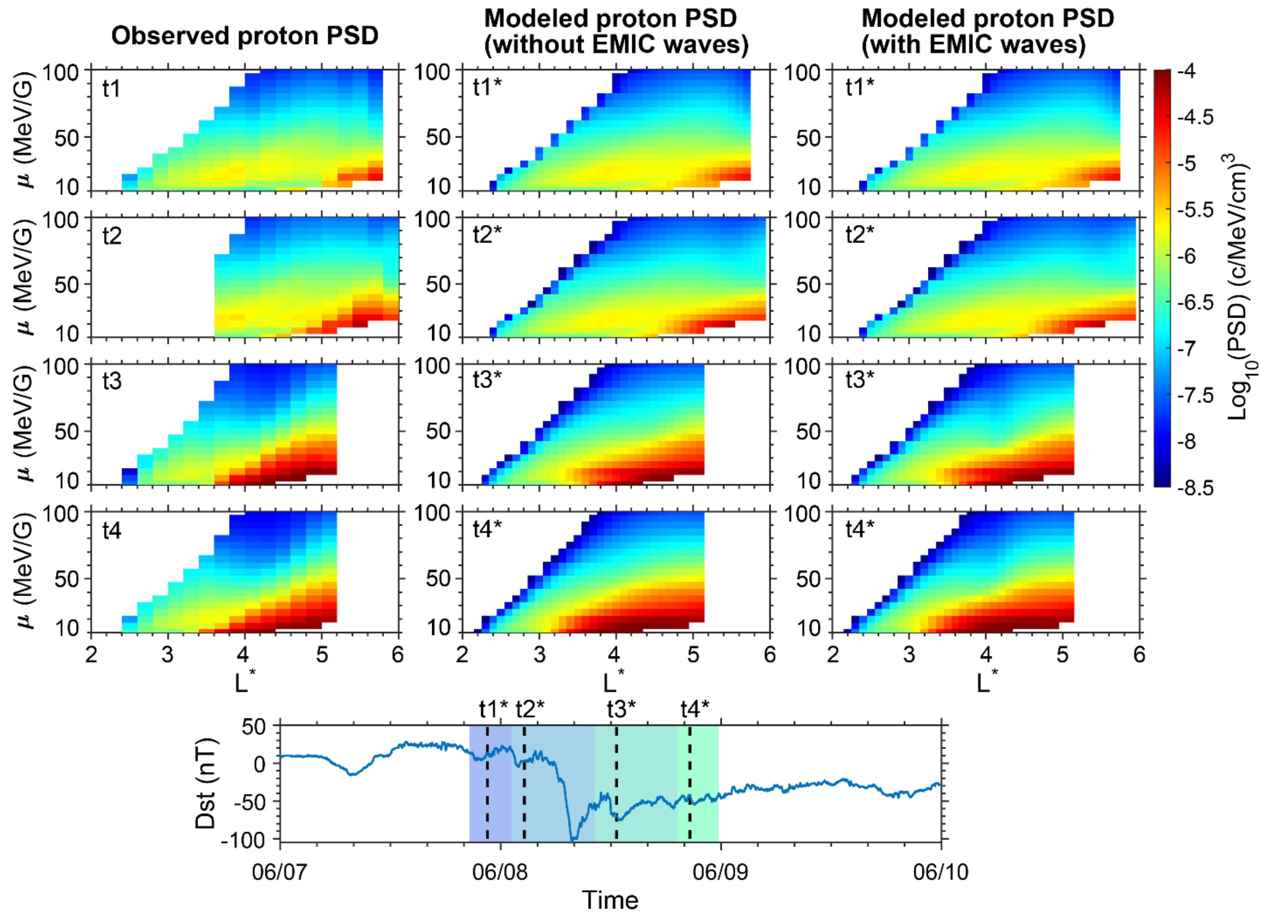

Figure 8. Comparison between the observed and modeled μ=10–100 MeV/G proton phase space density (PSD) during Event 1. Proton PSD is displayed as a function of L^* and μ for a specific period or epoch. For proton PSD observations on the left, the period marker corresponds to the shaded area in the bottom panel, while the epoch marker for the modeled proton PSD corresponds to the dashed line during the shaded period.

EMIC wave scattering loss contributes to weakening the deep penetration of ~40-100 MeV/G protons while the same μ electrons are not affected. In Figure 8, we present the comparison between observed and modeled proton PSD of multiple μ values from 10-100 MeV/G before, during and after the June 8 storm. In each subplot, the proton PSD is displayed as a function of L^* and μ. The time of the observations and simulations proceeds from top to bottom panels. The left column shows the observed proton PSD variations, the middle and right columns present the simulated proton PSD without or with EMIC wave losses, respectively. The Dst index is shown in the bottom panel. The labels 't1' to 't4' denote the averaged period for proton PSD observations, which are indicated by the shaded region in the bottom panel; '$t1^*$' to '$t4^*$' represent the simulation instants selected within the period of observations, which are marked by the black dashed lines. From t2 to t3, lower μ protons experience stronger inward transport than higher μ protons. The 'no-EMIC-loss' model performed well reproducing the μ-dependent storm-time enhancement and inward transport of proton PSD. However, as shown by the 't2' and 't3' of the observed proton PSD, there are some 'bite-out' losses for >60 MeV/G protons happening at L^* ~4.2 on 8 June 2015, which cannot be explained by the 'no-EMIC-loss' model. With the EMIC wave effects included, the right column of Figure 8 reproduces such local losses. While <35 MeV/G protons still undergo significant inward transport, the scattering loss due to EMIC waves becomes effective for protons > 35 MeV/G. PSD of >35 MeV/G protons decreased rapidly at L^*~4.2 from t2* to t3* and a clear local 'bite-out' feature formed for >60 MeV/G protons, which matches the observation well. As the modeling results suggest, in the absence of EMIC wave scattering loss, ~70 MeV/G protons might still experience inward deep penetration to L^*<4; while EMIC scattering effect leads to rapid local loss for relatively high μ protons that deter the deep penetration from extending to L^*<4.

4.2 Event 2 (2014 November 4 storm)

A second event, the 2014 November 4 storm, is also selected and modeled to verify that the bi-particle model can reproduce the different deep penetration of electrons and protons during other periods. Unlike Event 1, He+ band EMIC wave activities were not observed by RBSP during the November 4 storm. Therefore, EMIC wave scattering loss is not considered for this event and charge exchange loss is treated as the only loss mechanism for protons. Figure A1 in the appendix shows the model results for 20 MeV/G electrons and protons in the same format as Figure 6. The model captured the electron and proton inward penetrating dynamics to L<4 during the storm main phase. Distinctly from Event 1, the electron and proton PSD values at the beginning of the storm were at a relatively higher level, while the PSD radial profiles at the end of the modeled period became similar for both events. The different deep penetration of electrons and protons is clear from both observation and modeling results at L=3-3.5. In this L range, the electron PSD is enhanced by more than one order of magnitude, while proton PSD is not affected. This shows that the modeled 20 MeV/G electrons can penetrate inward to L<3.5 while protons at the same μ stop inward penetration at L>4. Figure A2 presents the proton model results from 10 to 100 MeV/G in a similar format as Figure 8. Observed PSD is shown in the left column and modeled PSD without EMIC scattering loss is on the right side. The deeper penetration of lower μ protons is well reproduced by the radial diffusion-convection model.

5. Discussion

In this study, we extend the energy-dependent convection-diffusion model for electrons by Mei et al. (2023) for protons using the same model but with different coefficients considering the relativistic effect and different loss mechanisms on electrons and protons. The bi-particle model performs well for both electrons and protons for the same events, capturing not only the μ-dependence of each species, but also the difference between the two species. To quantitatively compare how the relativistic effect will affect electrons and protons and lead to different inward transport, we assume that the ULF perturbations interacting with electrons or protons through drift resonance and leading to radial diffusion, are at the same level of intensity. Tong et al. (2024) statistically studied m>0 (eastward propagating) and m<0 (westward propagating) ULF waves based on GOES 13 and 15 measurements: their results showed that the peak values of power spectral density of the two waves are similar. We also considered the relativistic effect on radial convectional transport caused by time-varying large-scale electric fields. In Mei et al. (2023), such electric-field-induced inward transport was quantified by assuming symmetric large-scale electric fields, like the Volland-Stern model. We mainly discussed the contribution of symmetric large-scale electric fields to the different deep penetration of electrons and protons. More localized DC electric fields, like Subauroral Polarization Streams (SAPS) electric fields in radial direction (Califf et al., 2016; Califf et al., 2022; Lejosne et al., 2018; Lin et al., 2022; Zhao et al., 2017), might influence electrons and protons differently and are beyond the scope of this study.

Charge exchange and EMIC wave scattering are the two major loss mechanisms considered in the bi-particle model for protons. Charge exchange loss depends on the type of charge exchange, cross section area of protons as a function of energy, and neutral density in exosphere. We compared two types of charge exchange loss, H^+-H and H^+-O, and showed that the former dominates for radiation belt protons. We used the NRLMSIS 2.0 model to obtain the average hydrogen density at the exobase. Our results suggested that the neutral density variation during storm time does not significantly influence the loss timescales of proton at a fixed μ since the energy-dependence of charge exchange cross section dominates. Loss due to EMIC wave scattering is analyzed and quantified for a particular storm event, during which a localized 'bite-out' feature is clearly observed. EMIC wave activity at the same *L* range have been observed and reported by Hogan et al. (2023), thus we calculated the corresponding pitch angle diffusion coefficients and estimated proton lifetime to quantify the timescale of EMIC wave induced loss. Results suggest that EMIC waves play a significant role in scattering relatively higher μ (>60 MeV/G) protons, which prevent them from further penetrating to lower *L*, while lower μ (<30 MeV/G) protons below the minimum resonant energy are not affected. This is consistent with the decreased occurrence of events where deep penetration of protons is observed as μ increases revealed by Zhao et al. (2023), which showed that while ~70 deep penetration events of 10 MeV/G protons to $L<4$ were observed over 6 years, very few deep penetration events could be identified for $\mu > 20$ MeV/G. Such a drastic decrease does not exist in electron observations at the same μ, which is consistent with our results that these electrons are outside the resonant region with the observed EMIC waves. Therefore, EMIC wave scattering loss contributes to the sudden drop of proton deep penetration occurrence at high μ.

6. Conclusion

As suggested by previous statistical studies, electrons and protons respond differently to geomagnetic storms in terms of their inward penetration depth, time scale and energy-dependence. Considering that the radial transport due to enhanced large-scale electric fields is a significant mechanism for trapped particles to penetrate to $L<4$, one would expect that the electrons and protons will equally respond to the electric fields and behave similarly. In this study, we considered the relativistic effects on radial transport and different loss mechanisms for electrons and protons in a bi-particle convection-diffusion model and showed that this model can be used to reproduce both deep penetrations of electrons and protons. Based on our modeling results, here we provide explanations for the different dynamic variations for electrons and protons:

1. Due to the relativistic effect, electrons drift slower than protons at the same energy, which results in stronger radial diffusion and convection that the protons experience. The drift period

difference becomes greater as μ increases or *L* decreases, thus protons at μ>50 MeV/G tend to stop their inward transport at higher *L* than the electrons, while 10 MeV/G electrons and protons have more similar dynamics. This is consistent with the statistical results from a previous study which showed that 10 MeV/G proton deep penetration to *L*<4 is less frequently than electron but still happens, while >20 MeV/G proton deep penetration to *L*<4 is very rare (Zhao et al., 2023).

2. EMIC wave scattering loss is quantified and applied to the model for a specific event, during which EMIC wave activity has been observed by RBSP and reported by previous studies. Modeling results suggest that during the event, EMIC waves can rapidly scatter 100s of keV protons at *L*~4.2 on timescales of ~0.1-0.7 day. Such a rapid local loss process prevents the high-energy protons from being inward transported to lower *L* and creates a local 'bite-out' feature. On the other hand, 100s of keV electrons are shown to be outside of the resonant region with the observed EMIC wave, based on computed minimum resonant energies.

Appendix

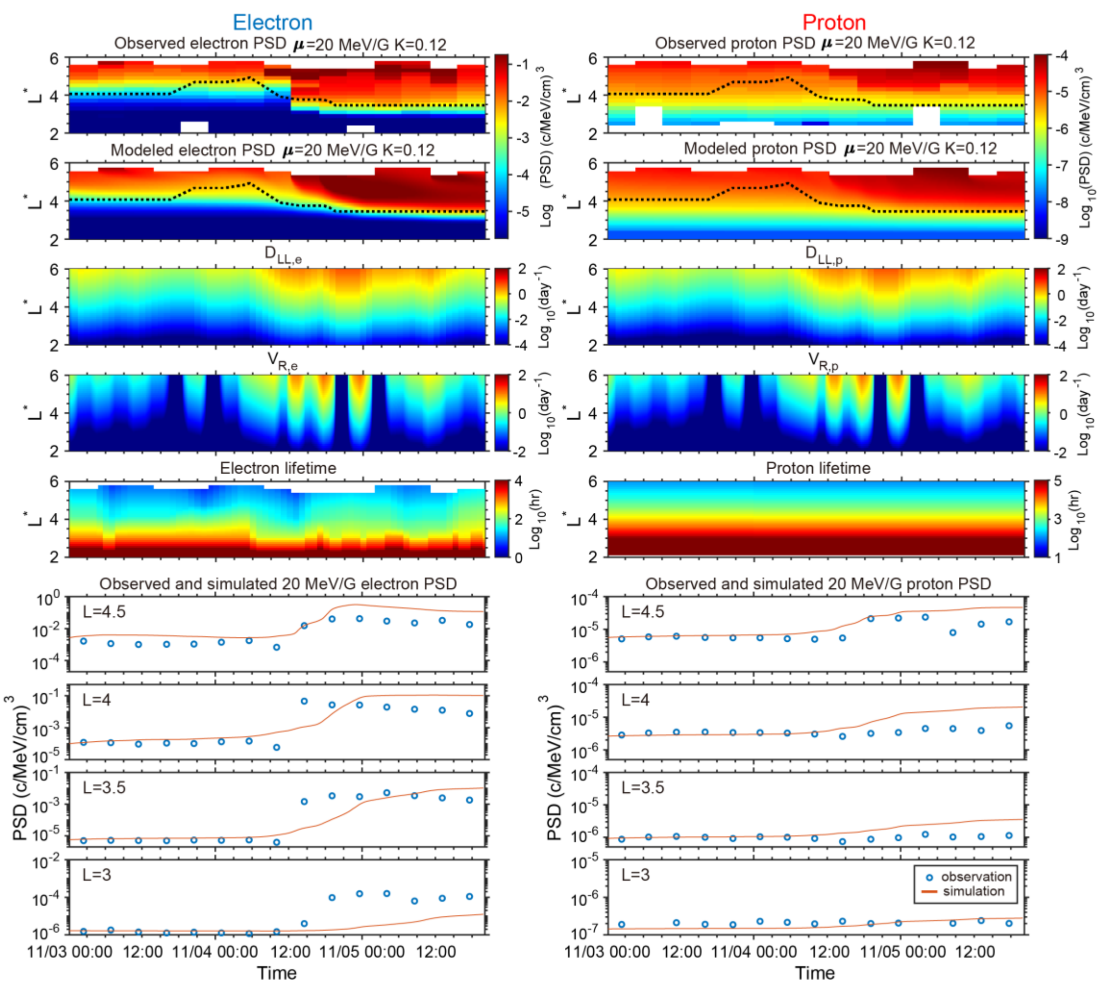

Figure A1. Modeling results for 20 MeV/G electron (left column) and proton (right column) during event 2.

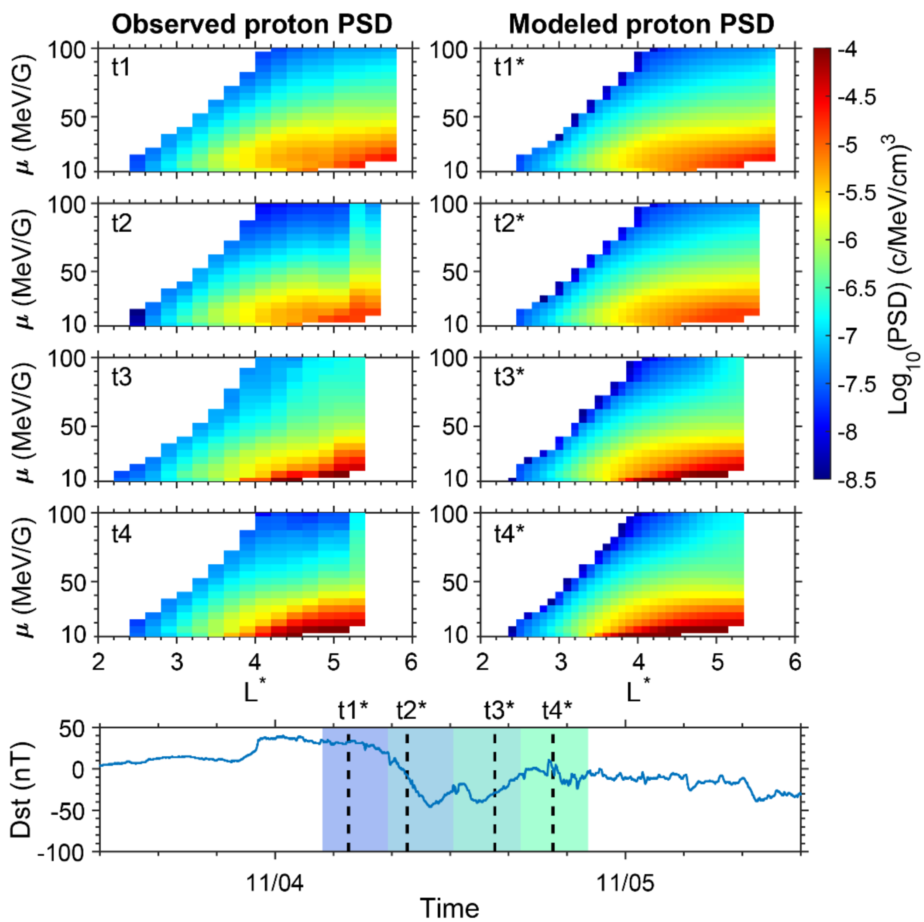

Figure A2. Comparison between the observed and modeled proton phase space density (PSD) for μ=10–100 MeV/G during Event 2 in the same format of Figure 8. Modeled PSD < $10^{-8.5}$ $(c/MeV/cm)^3$ is not shown.

Acknowledgements

This work was supported by NASA Grant 80NSSC21K0583 and NSF Grant AGS 1834971. H. Zhao was supported by the NSF Grant AGS 2131012, 2140934, 2338125, and NASA Grant 80NSSC22K0356. We acknowledge the developers of NRLMSIS 2.0 model and the Community Coordinated Modeling Center (CCMC) for providing simulation results of exobase used in this study.

Data Availability Statement

We acknowledge the Van Allen Probes mission, particularly the ECT team for providing the particle data. Processing and analysis of the MagEIS data was supported by Energetic Particle, Composition, and Thermal Plasma (RBSP-ECT) investigation funded under NASA's Prime

contract no. NAS5-01072. All RBSP-ECT data are publicly available at https://rbsp-ect.newmexicoconsortium.org/science/DataDirectories.php.

Reference

Baker, D. N., Kanekal, S. G., Hoxie, V., Li, X., Jaynes, A. N., Zhao, H., et al. (2021). The Relativistic Electron-Proton Telescope (REPT) Investigation: Design, Operational Properties, and Science Highlights. *Space Science Reviews, 217*(5).

Baker, D. N., Kanekal, S. G., Li, X., Monk, S. P., Goldstein, J., & Burch, J. L. (2004). An extreme distortion of the Van Allen belt arising from the 'Hallowe'en' solar storm in 2003. *Nature, 432*(7019), 878-881. https://doi.org/10.1038/nature03116

Blake, J. B., Carranza, P. A., Claudepierre, S. G., Clemmons, J. H., Crain, W. R., Dotan, Y., et al. (2013). The Magnetic Electron Ion Spectrometer (MagEIS) Instruments Aboard the Radiation Belt Storm Probes (RBSP) Spacecraft. *Space Science Reviews, 179*(1-4), 383-421.

Califf, S., Li, X., Wolf, R. A., Zhao, H., Jaynes, A. N., Wilder, F. D., et al. (2016). Large‐amplitude electric fields in the inner magnetosphere: Van Allen Probes observations of subauroral polarization streams. *Journal of Geophysical Research: Space Physics, 121*(6), 5294-5306.

Califf, S., Li, X., Zhao, H., Kellerman, A., Sarris, T. E., Jaynes, A., & Malaspina, D. M. (2017). The role of the convection electric field in filling the slot region between the inner and outer radiation belts. *Journal of Geophysical Research: Space Physics, 122*(2), 2051-2068.

Califf, S., Zhao, H., Gkioulidou, M., Manweiler, J. W., Mitchell, D. G., & Tian, S. (2022). Multi‐Event Study on the Connection Between Subauroral Polarization Streams and Deep Energetic Particle Injections in the Inner Magnetosphere. *Journal of Geophysical Research: Space Physics, 127*(2).

Carpenter, D. L., & Anderson, R. R. (1992). An ISEE/whistler model of equatorial electron density in the magnetosphere. *Journal of Geophysical Research, 97*(A2), 1097-1108. https://agupubs.onlinelibrary.wiley.com/doi/abs/10.1029/91JA01548

Chamberlain, J. W. (1963). Planetary Coronae and Atmospheric Evaporation. *Planetary and Space Science, 11*(8), 901-960. <Go to ISI>://WOS:A1963XD58900005

Emmert, J. T., Drob, D. P., Picone, J. M., Siskind, D. E., Jones, M., Mlynczak, M. G., et al. (2021). NRLMSIS 2.0: A Whole‐Atmosphere Empirical Model of Temperature and Neutral Species Densities. *Earth and Space Science, 8*(3).

Engebretson, M. J., Posch, J. L., Braun, D. J., Li, W., Ma, Q., Kellerman, A. C., et al. (2018). EMIC Wave Events During the Four GEM QARBM Challenge Intervals. *Journal of Geophysical Research: Space Physics, 123*(8), 6394-6423.

Fok, M. C., Kozyra, J. U., Nagy, A. F., & Cravens, T. E. (1991). Lifetime of ring current particles due to coulomb collisions in the plasmasphere. *Journal of Geophysical Research, 96*(A5).

Gkioulidou, M., Ohtani, S., Mitchell, D. G., Ukhorskiy, A. Y., Reeves, G. D., Turner, D. L., et al. (2015). Spatial structure and temporal evolution of energetic particle injections in the inner magnetosphere during the 14 July 2013 substorm event. *Journal of Geophysical Research: Space Physics, 120*(3), 1924-1938.

Gkioulidou, M., Ukhorskiy, A. Y., Mitchell, D. G., & Lanzerotti, L. J. (2016). Storm time dynamics of ring current protons: Implications for the long‐term energy budget in the inner magnetosphere. *Geophysical Research Letters, 43*(10), 4736-4744.

Gkioulidou, M., Ukhorskiy, A. Y., Mitchell, D. G., Sotirelis, T., Mauk, B. H., & Lanzerotti, L. J. (2014). The role of small‐scale ion injections in the buildup of Earth's ring current pressure: Van Allen Probes observations of the 17 March 2013 storm. *Journal of Geophysical Research: Space Physics, 119*(9), 7327-7342.

Hamilton, D. C., Gloeckler, G., Ipavich, F. M., Stüdemann, W., Wilken, B., & Kremser, G. (1988). Ring current development during the great geomagnetic storm of February 1986. *Journal of Geophysical Research, 93*(A12).

Hogan, B., Li, X., Xiang, Z., Zhao, H., Mei, Y., O'Brien, D., et al. (2023). On the Dynamics of Ultrarelativistic Electrons (>2 MeV) Near L* = 3.5 During 8 June 2015. *Journal of Geophysical Research: Space Physics, 128*(11).

Jordanova, V. K., Albert, J., & Miyoshi, Y. (2008). Relativistic electron precipitation by EMIC waves from self - consistent global simulations. *Journal of Geophysical Research: Space Physics, 113*(A3).

Jordanova, V. K., Farrugia, C. J., Thorne, R. M., Khazanov, G. V., Reeves, G. D., & Thomsen, M. F. (2001). Modeling ring current proton precipitation by electromagnetic ion cyclotron waves during the May 14–16, 1997, storm. *Journal of Geophysical Research: Space Physics, 106*(A1), 7-22.

Keika, K., Nosé, M., Brandt, P. C., Ohtani, S., Mitchell, D. G., & Roelof, E. C. (2006). Contribution of charge exchange loss to the storm time ring current decay: IMAGE/HENA observations. *Journal of Geophysical Research, 111*(A11).

Kersten, T., Horne, R. B., Glauert, S. A., Meredith, N. P., Fraser, B. J., & Grew, R. S. (2014). Electron losses from the radiation belts caused by EMIC waves. *Journal of Geophysical Research: Space Physics, 119*(11), 8820-8837.

Khoo, L. Y., Li, X., Zhao, H., Sarris, T. E., Xiang, Z., Zhang, K., et al. (2018). On the Initial Enhancement of Energetic Electrons and the Innermost Plasmapause Locations: Coronal Mass Ejection - Driven Storm Periods. *Journal of Geophysical Research: Space Physics, 123*(11), 9252-9264.

Khoo, L. Y., Li, X., Zhao, H., Thaller, S. A., & Hogan, B. (2021). Multi - Event Studies of Sudden Energetic Electron Enhancements in the Inner Magnetosphere and Its Association With Plasmapause Positions. *Journal of Geophysical Research: Space Physics, 126*(11).

Kistler, L. M., Ipavich, F. M., Hamilton, D. C., Gloeckler, G., Wilken, B., Kremser, G., & Stüdemann, W. (1989). Energy spectra of the major ion species in the ring current during geomagnetic storms. *Journal of Geophysical Research, 94*(A4).

Lejosne, S., Kunduri, B. S. R., Mozer, F. S., & Turner, D. L. (2018). Energetic Electron Injections Deep Into the Inner Magnetosphere: A Result of the Subauroral Polarization Stream (SAPS) Potential Drop. *Geophysical Research Letters, 45*(9), 3811-3819.

Lenchek, A. M., S. F. Singer, and R. C. Wentworth (1961), Geomagnetically trapped electrons from cosmic ray albedo neutrons, *J. Geophys. Res.*, 66(12), 4027–4046, doi:10.1029/JZ066i012p04027.

Li, X., Baker, D. N., O'Brien, T. P., Xie, L., & Zong, Q. G. (2006). Correlation between the inner edge of outer radiation belt electrons and the innermost plasmapause location. *Geophysical Research Letters, 33*(14), L14107.

Lin, D., Wang, W., Merkin, V. G., Huang, C., Oppenheim, M., Sorathia, K., et al. (2022). Origin of Dawnside Subauroral Polarization Streams During Major Geomagnetic Storms. *AGU Advances, 3*(4).

Lindsay, B. G., & Stebbings, R. F. (2005). Charge transfer cross sections for energetic neutral atom data analysis. *Journal of Geophysical Research: Space Physics, 110*(A12).

Liu, W., Tu, W., Li, X., Sarris, T., Khotyaintsev, Y., Fu, H., et al. (2016). On the calculation of electric diffusion coefficient of radiation belt electrons with in situ electric field measurements by THEMIS. *Geophysical Research Letters, 43*(3), 1023-1030.

Lyu, X., Ma, Q., Tu, W., Li, W., & Capannolo, L. (2022). Modeling the Simultaneous Dropout of Energetic Electrons and Protons by EMIC Wave Scattering. *Geophysical Research Letters, 49*(20).

Lyu, X., & Tu, W. (2022). Modeling the Dynamics of Energetic Protons in Earth's Inner Magnetosphere. *Journal of Geophysical Research: Space Physics, 127*(3).

Mauk, B. H., Fox, N. J., Kanekal, S. G., Kessel, R. L., Sibeck, D. G., & Ukhorskiy, A. (2013). Science Objectives and Rationale for the Radiation Belt Storm Probes Mission. *Space Science Reviews, 179*(1-4), 3-27.

Mei, Y., Li, X., Zhao, H., Sarris, T., Khoo, L., Hogan, B., et al. (2023). On the Energy‐Dependent Deep (L < 3.5) Penetration of Radiation Belt Electrons. *Geophysical Research Letters, 50*(10).

Meredith, N. P., Horne, R. B., Glauert, S. A., Thorne, R. M., Summers, D., Albert, J. M., & Anderson, R. R. (2006). Energetic outer zone electron loss timescales during low geomagnetic activity. *Journal of Geophysical Research: Space Physics, 111*(A5).

Mitchell, D. G., Lanzerotti, L. J., Kim, C. K., Stokes, M., Ho, G., Cooper, S., et al. (2013). Radiation Belt Storm Probes Ion Composition Experiment (RBSPICE). *Space Science Reviews, 179*(1-4), 263-308.

Ni, B., Cao, X., Zou, Z., Zhou, C., Gu, X., Bortnik, J., et al. (2015). Resonant scattering of outer zone relativistic electrons by multiband EMIC waves and resultant electron loss time scales. *Journal of Geophysical Research: Space Physics, 120*(9), 7357-7373.

Ni, B., Thorne, R. M., Meredith, N. P., Horne, R. B., & Shprits, Y. Y. (2011). Resonant scattering of plasma sheet electrons leading to diffuse auroral precipitation: 2. Evaluation for whistler mode chorus waves. *Journal of Geophysical Research: Space Physics, 116*(A4), n/a-n/a.

Ni, B., Thorne, R. M., Shprits, Y. Y., & Bortnik, J. (2008). Resonant scattering of plasma sheet electrons by whistler-mode chorus: Contribution to diffuse auroral precipitation. *Geophysical Research Letters, 35*(11).

Ni, B., Zhang, Y., & Gu, X. (2023). Identification of ring current proton precipitation driven by scattering of electromagnetic ion cyclotron waves. *Fundamental Research, 3*(2), 257-264.

Orlova, K., & Shprits, Y. (2014). Model of lifetimes of the outer radiation belt electrons in a realistic magnetic field using realistic chorus wave parameters. *Journal of Geophysical Research: Space Physics, 119*(2), 770-780.

Qin, M., Hudson, M., Li, Z., Millan, R., Shen, X., Shprits, Y., et al. (2019). Investigating Loss of Relativistic Electrons Associated With EMIC Waves at Low L Values on 22 June 2015. *Journal of Geophysical Research: Space Physics, 124*(6), 4022-4036.

Reeves, G. D., Friedel, R. H., Larsen, B. A., Skoug, R. M., Funsten, H. O., Claudepierre, S. G., et al. (2016). Energy-dependent dynamics of keV to MeV electrons in the inner zone, outer zone, and slot regions. *Journal of Geophysical Research: Space Physics, 121*(1), 397-412. https://www.ncbi.nlm.nih.gov/pubmed/27818855

Roederer, J. G. (1970). *Dynamics of geomagnetically trapped radiation*. Springer-Verlag.

Schulz, M., & Lanzerotti, L. J. (1974). Adiabatic Invariants and Magnetospheric Models. In M. Schulz & L. J. Lanzerotti (Eds.), *Particle Diffusion in the Radiation Belts* (pp. 10-45). Berlin, Heidelberg: Springer Berlin Heidelberg.

Sheeley, B. W., Moldwin, M. B., Rassoul, H. K., & Anderson, R. R. (2001). An empirical plasmasphere and trough density model: CRRES observations. *Journal of Geophysical Research: Space Physics, 106*(A11), 25631-25641.

Sheldon, R. B., & Hamilton, D. C. (1993). Ion transport and loss in the Earth's quiet ring current: 1. Data and standard model. *Journal of Geophysical Research: Space Physics, 98*(A8), 13491-13508.

Shprits, Y., Drozdov, A. Y., Spasojevic, M., Kellerman, A. C., Usanova, M. E., Engebretson, M. J., et al. (2016). Wave-induced loss of ultra-relativistic electrons in the Van Allen radiation belts. *Nat Commun, 7*, 12883. https://www.ncbi.nlm.nih.gov/pubmed/27678050

Shprits, Y., Kellerman, A., Aseev, N., Drozdov, A. Y., & Michaelis, I. (2017). Multi‐MeV electron loss in the heart of the radiation belts. *Geophysical Research Letters, 44*(3), 1204-1209.

Shprits, Y., & Ni, B. (2009). Dependence of the quasi‐linear scattering rates on the wave normal distribution of chorus waves. *Journal of Geophysical Research: Space Physics, 114*(A11).

Smith, P. H., & Bewtra, N. K. (1978). Charge-Exchange Lifetimes for Ring Current Ions. *Space Science Reviews, 22*(3), 301-318. <Go to ISI>://WOS:A1978GF13200002

Smith, P. H., Hoffman, R. A., & Fritz, T. A. (1976). Ring current proton decay by charge exchange. *Journal of Geophysical Research, 81*(16), 2701-2708.

Spence, H. E., Reeves, G. D., Baker, D. N., Blake, J. B., Bolton, M., Bourdarie, S., et al. (2013). Science Goals and Overview of the Radiation Belt Storm Probes (RBSP) Energetic Particle, Composition, and Thermal Plasma (ECT) Suite on NASA's Van Allen Probes Mission. *Space Science Reviews, 179*(1-4), 311-336.

Summers, D., Ni, B., & Meredith, N. P. (2007). Timescales for radiation belt electron acceleration and loss due to resonant wave‐particle interactions: 1. Theory. *Journal of Geophysical Research: Space Physics, 112*(A4).

Thorne, R. M., Li, W., Ni, B., Ma, Q., Bortnik, J., Baker, D. N., et al. (2013). Evolution and slow decay of an unusual narrow ring of relativistic electrons near L ~ 3.2 following the September 2012 magnetic storm. *Geophysical Research Letters, 40*(14), 3507-3511. https://agupubs.onlinelibrary.wiley.com/doi/abs/10.1002/grl.50627

Tong, X., Liu, W., Zhang, D., Sarris, T., Li, X., Zhang, Z., & Yan, L. (2024). Statistical Study on the Azimuthal Mode Number of Pc5 ULF Wave in the Inner Magnetosphere. *Journal of Geophysical Research: Space Physics, 129*(2).

Tsyganenko, N. A., & Sitnov, M. I. (2005). Modeling the dynamics of the inner magnetosphere during strong geomagnetic storms. *Journal of Geophysical Research-Space Physics, 110*(A3). <Go to ISI>://WOS:000227880500007

Turner, D. L., O'Brien, T. P., Fennell, J. F., Claudepierre, S. G., Blake, J. B., Jaynes, A. N., et al. (2017). Investigating the source of near‐relativistic and relativistic electrons in Earth's inner radiation belt. *Journal of Geophysical Research: Space Physics, 122*(1), 695-710.

Usanova, M. E., Mann, I. R., Kale, Z. C., Rae, I. J., Sydora, R. D., Sandanger, M., et al. (2010). Conjugate ground and multisatellite observations of compression‐related EMIC Pc1 waves and associated proton precipitation. *Journal of Geophysical Research: Space Physics, 115*(A7).

Xiang, Z., Tu, W., Li, X., Ni, B., Morley, S. K., & Baker, D. N. (2017). Understanding the Mechanisms of Radiation Belt Dropouts Observed by Van Allen Probes. *Journal of Geophysical Research: Space Physics, 122*(10), 9858-9879.

Zhao, H., Baker, D. N., Califf, S., Li, X., Jaynes, A. N., Leonard, T., et al. (2017). Van Allen Probes Measurements of Energetic Particle Deep Penetration Into the Low L Region (L < 4) During the Storm on 8 April 2016. *Journal of Geophysical Research: Space Physics, 122*(12).

Zhao, H., Califf, S. T., Goyal, R., Li, X., Gkioulidou, M., Manweiler, J. W., & Krantz, S. (2023). Statistical Analysis of the Differential Deep Penetration of Energetic Electrons and Protons into the Low L Region (L < 4). *Journal of Geophysical Research: Space Physics, 128*(4).

Zhao, H., & Li, X. (2013). Modeling energetic electron penetration into the slot region and inner radiation belt. *Journal of Geophysical Research: Space Physics, 118*(11), 6936-6945. https://agupubs.onlinelibrary.wiley.com/doi/abs/10.1002/2013JA019240

Zhao, H., Li, X., Baker, D. N., Fennell, J. F., Blake, J. B., Larsen, B. A., et al. (2015). The evolution of ring current ion energy density and energy content during geomagnetic storms based on Van Allen Probes measurements. *Journal of Geophysical Research: Space Physics, 120*(9), 7493-7511.

Zhu, Q., Cao, X., Gu, X., Ni, B., Xiang, Z., Fu, S., et al. (2021). Empirical Loss Timescales of Slot Region Electrons due to Plasmaspheric Hiss Based on Van Allen Probes Observations. *Journal of Geophysical Research: Space Physics, 126*(4).

Figure 1.

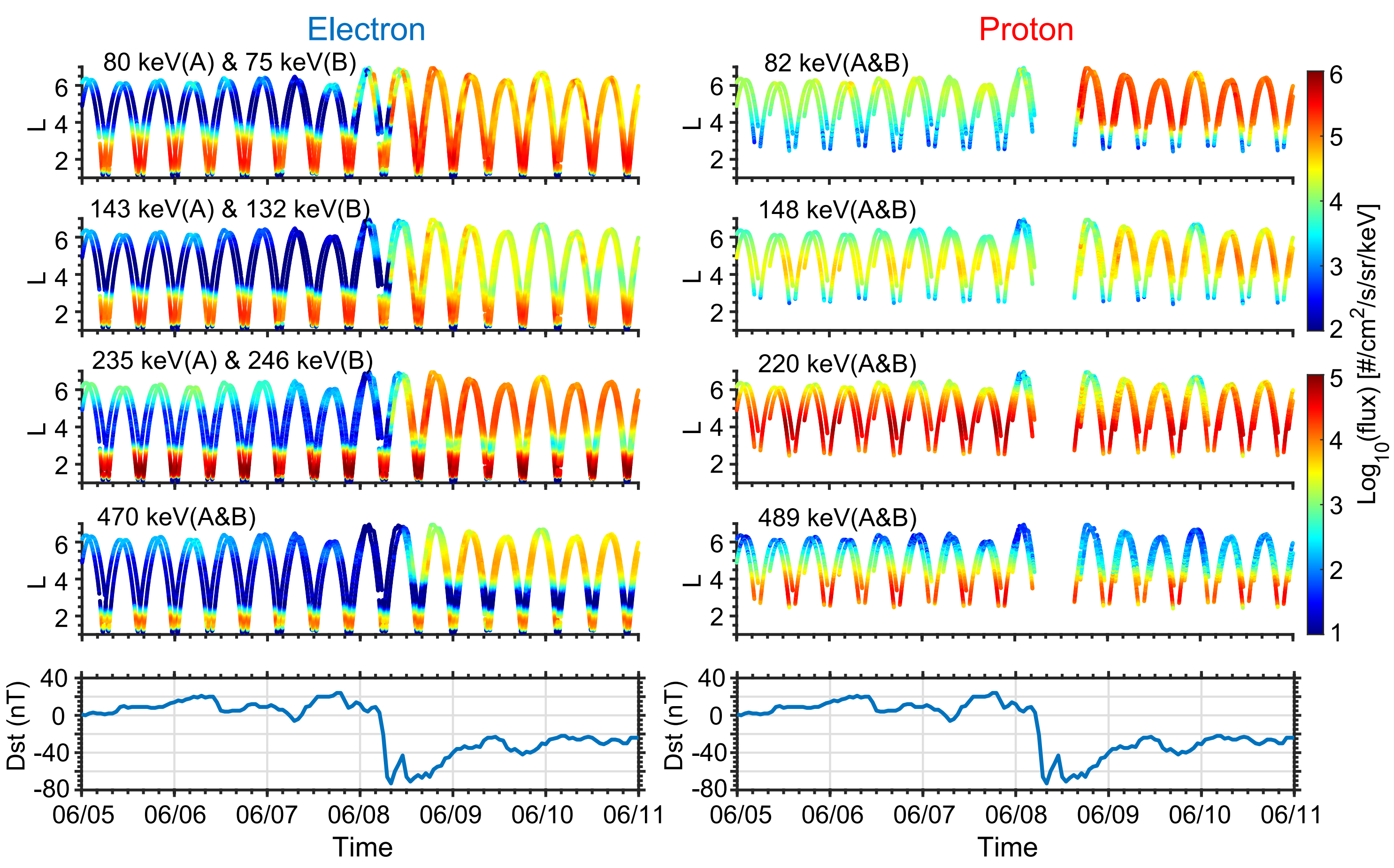
Electron
Proton
80 keV(A) & 75 keV(B)
143 keV(A) & 132 keV(B)
235 keV(A) & 246 keV(B)
470 keV(A&B)
82 keV(A&B)
148 keV(A&B)
220 keV(A&B)
489 keV(A&B)
L
Dst (nT)
Time
06/05
06/06
06/07
06/08
06/09
06/10
06/11
Log10(flux) [#/cm2/s/sr/keV]

Figure 2.

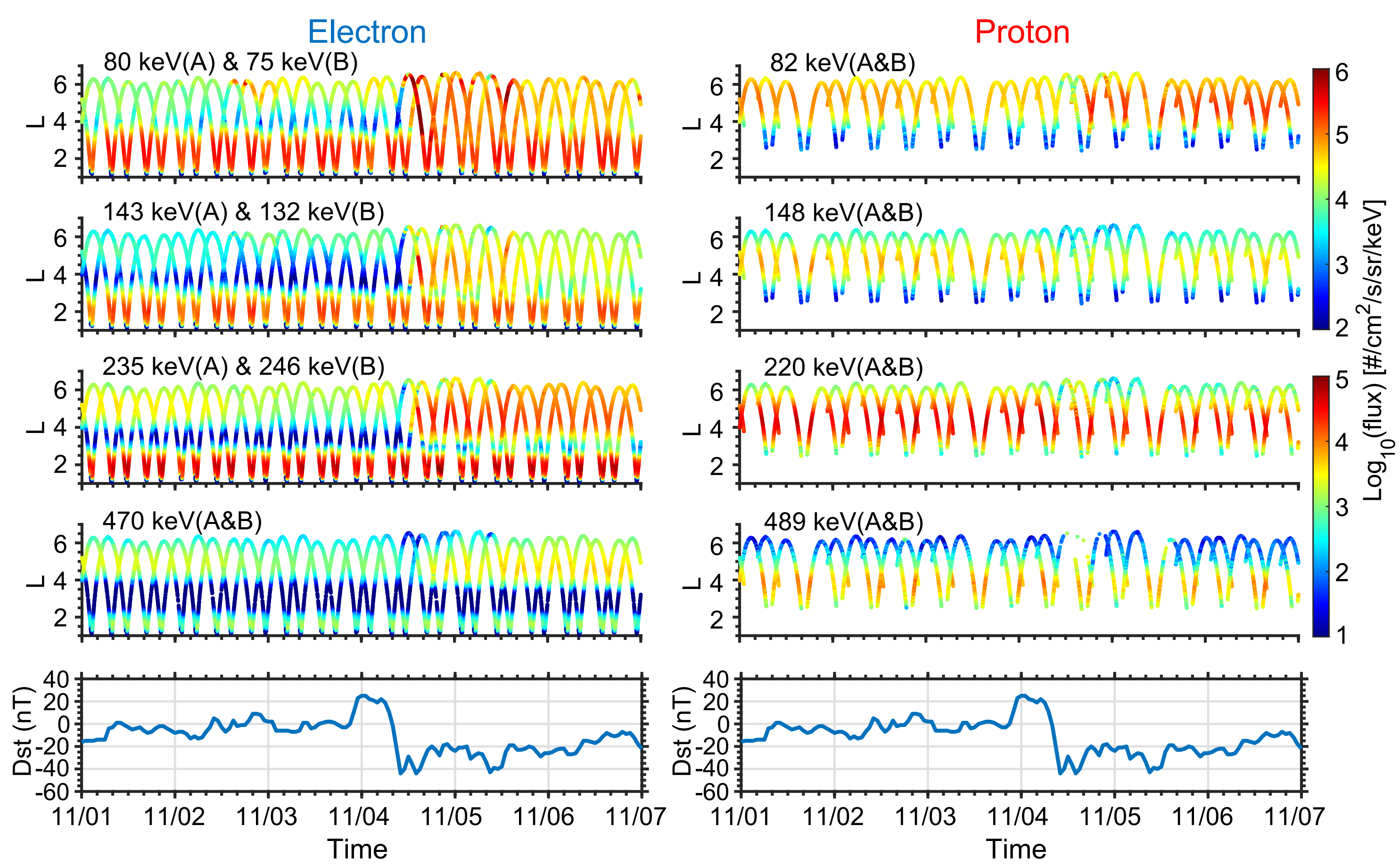

Electron
Proton
80 keV(A) & 75 keV(B)
143 keV(A) & 132 keV(B)
235 keV(A) & 246 keV(B)
470 keV(A&B)
82 keV(A&B)
148 keV(A&B)
220 keV(A&B)
489 keV(A&B)
L
Dst (nT)
Time
11/01
11/02
11/03
11/04
11/05
11/06
11/07
Log10(flux) [#/cm2/s/sr/keV]

Figure 3.

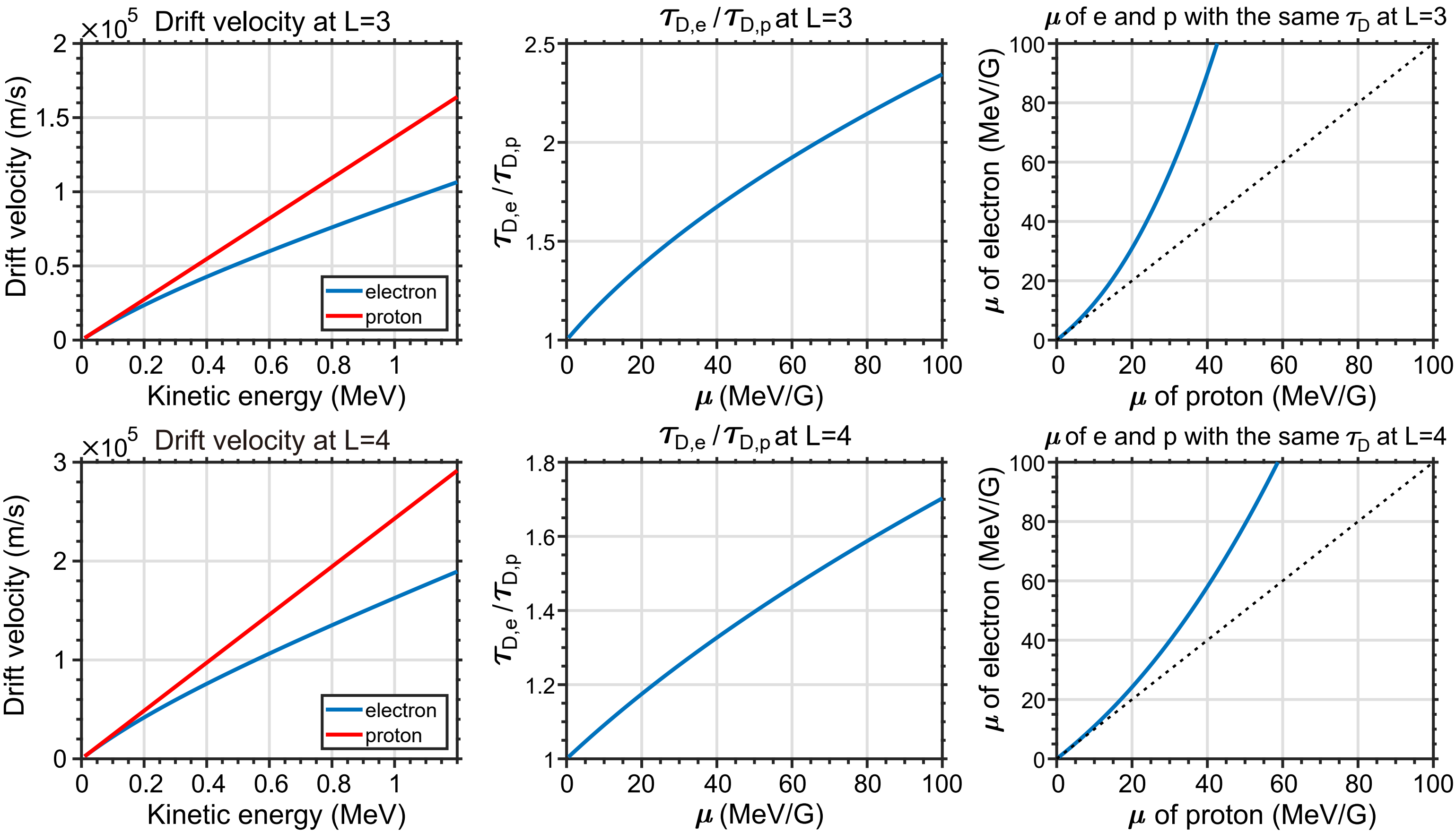

×10^5 Drift velocity at L=3
Drift velocity (m/s)
Kinetic energy (MeV)
electron
proton
τD,e / τD,p at L=3
τD,e / τD,p
μ (MeV/G)
μ of e and p with the same τD at L=3
μ of electron (MeV/G)
μ of proton (MeV/G)
×10^5 Drift velocity at L=4
Drift velocity (m/s)
Kinetic energy (MeV)
electron
proton
τD,e / τD,p at L=4
τD,e / τD,p
μ (MeV/G)
μ of e and p with the same τD at L=4
μ of electron (MeV/G)
μ of proton (MeV/G)

Figure4.

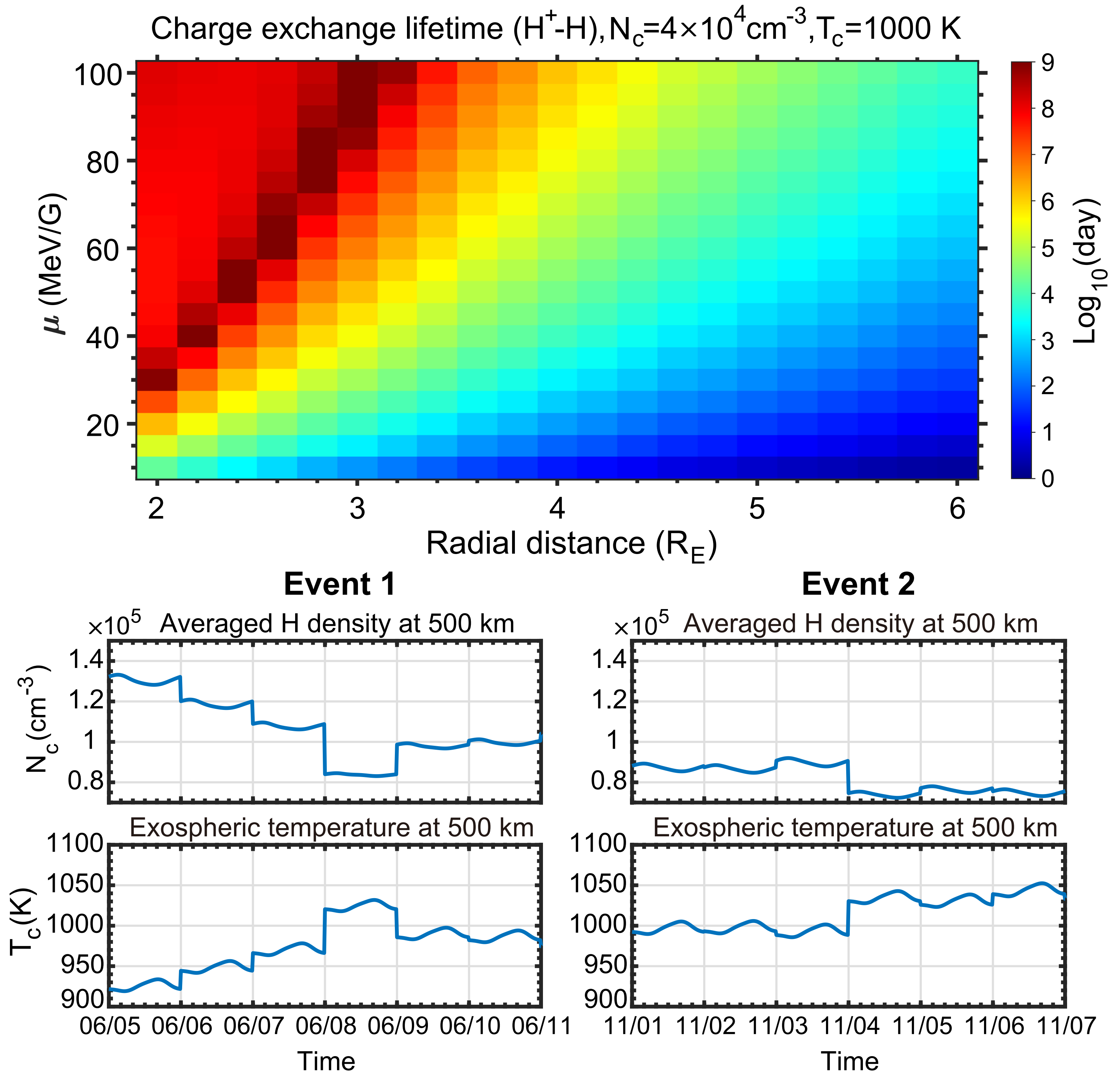
Charge exchange lifetime (H+-H), Nc=4×10^4 cm^-3, Tc=1000 K
μ (MeV/G)
Radial distance (RE)
Log10(day)
Event 1
Event 2
×10^5 Averaged H density at 500 km
Nc (cm^-3)
Exospheric temperature at 500 km
Tc(K)
06/05 06/06 06/07 06/08 06/09 06/10 06/11
11/01 11/02 11/03 11/04 11/05 11/06 11/07
Time

Figure 5.

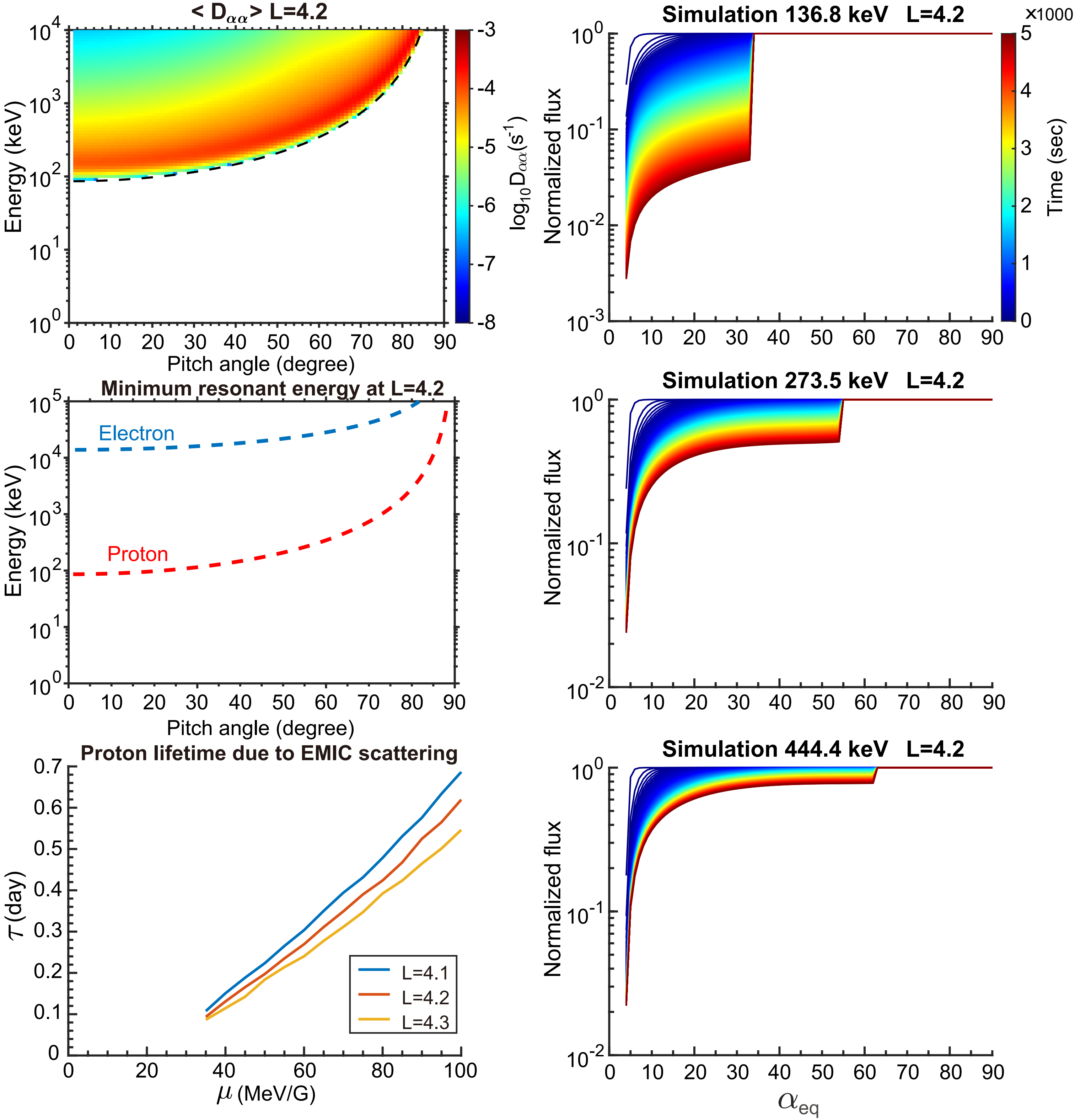

< $D_{\alpha\alpha}$ > L=4.2
Energy (keV)
Pitch angle (degree)
$\log_{10} D_{\alpha\alpha}(s^{-1})$
Simulation 136.8 keV L=4.2
Normalized flux
Time (sec)
×1000
Minimum resonant energy at L=4.2
Electron
Proton
Energy (keV)
Pitch angle (degree)
Simulation 273.5 keV L=4.2
Normalized flux
Proton lifetime due to EMIC scattering
τ (day)
μ (MeV/G)
L=4.1
L=4.2
L=4.3
Simulation 444.4 keV L=4.2
Normalized flux
α_{eq}

Figure6.

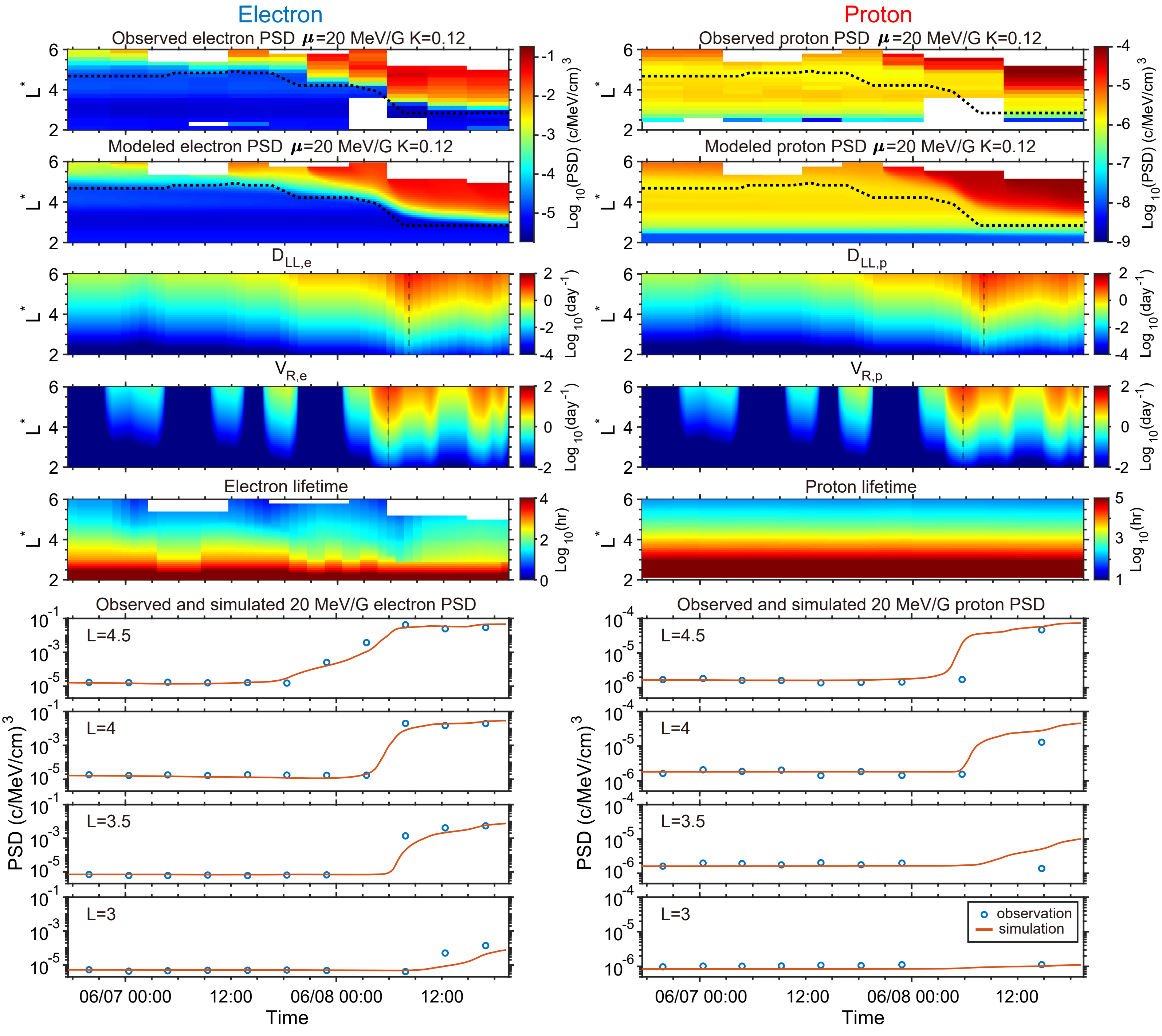

Electron
Proton
Observed electron PSD μ=20 MeV/G K=0.12
Observed proton PSD μ=20 MeV/G K=0.12
Modeled electron PSD μ=20 MeV/G K=0.12
Modeled proton PSD μ=20 MeV/G K=0.12
Log10(PSD) (c/MeV/cm)3
D_LL,e
D_LL,p
V_R,e
V_R,p
Log10(day-1)
Electron lifetime
Proton lifetime
Log10(hr)
L*
Observed and simulated 20 MeV/G electron PSD
Observed and simulated 20 MeV/G proton PSD
L=4.5
L=4
L=3.5
L=3
PSD (c/MeV/cm)3
observation
simulation
06/07 00:00
12:00
06/08 00:00
12:00
Time

Figure7.

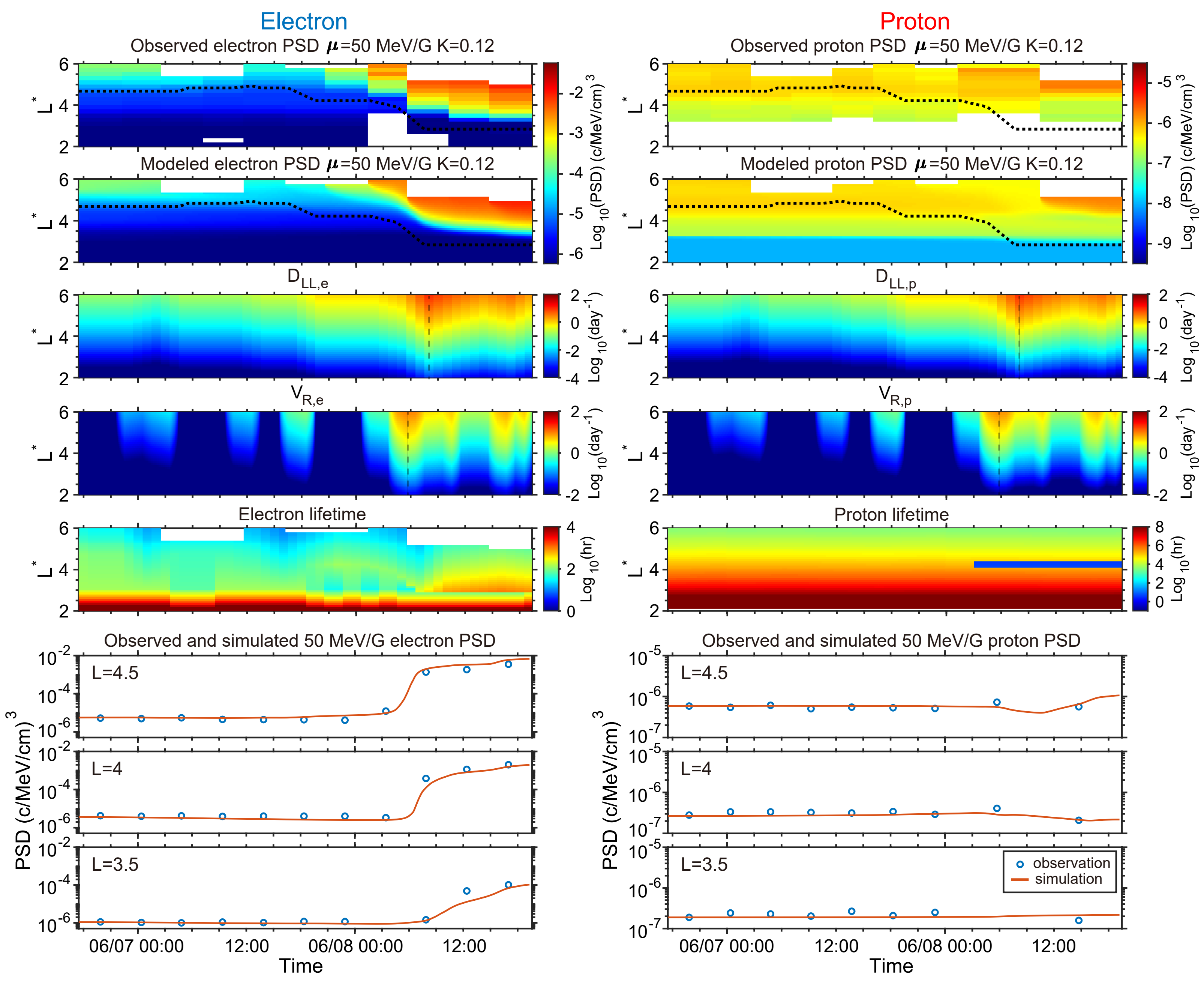

Electron
Proton
Observed electron PSD μ=50 MeV/G K=0.12
Observed proton PSD μ=50 MeV/G K=0.12
Modeled electron PSD μ=50 MeV/G K=0.12
Modeled proton PSD μ=50 MeV/G K=0.12
Log10(PSD) (c/MeV/cm)3
D_LL,e
D_LL,p
V_R,e
V_R,p
Log10(day-1)
Electron lifetime
Proton lifetime
Log10(hr)
L*
Observed and simulated 50 MeV/G electron PSD
Observed and simulated 50 MeV/G proton PSD
L=4.5
L=4
L=3.5
PSD (c/MeV/cm)3
observation
simulation
06/07 00:00
12:00
06/08 00:00
12:00
Time

Figure 8.

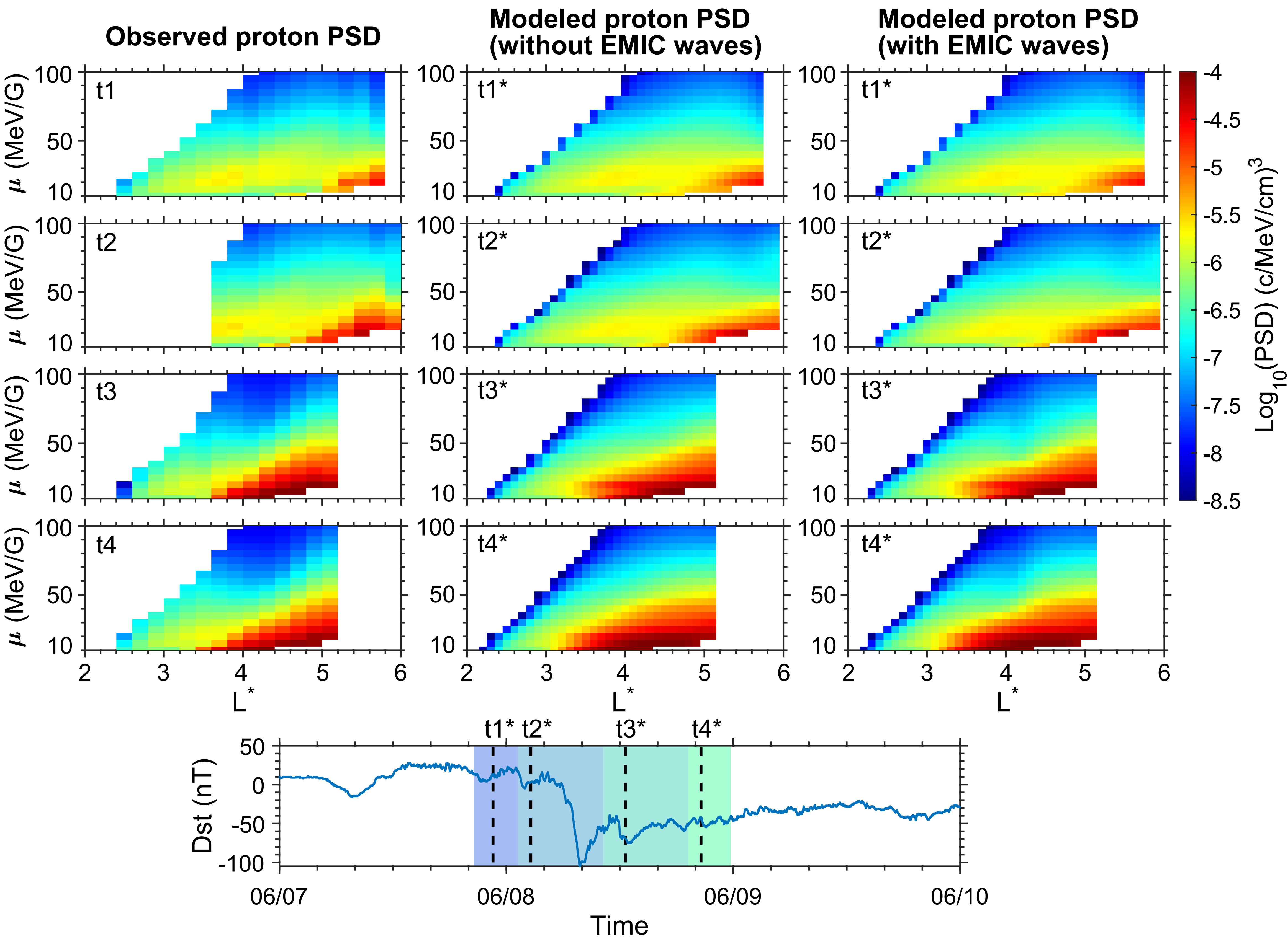

Observed proton PSD
Modeled proton PSD (without EMIC waves)
Modeled proton PSD (with EMIC waves)
t1
t2
t3
t4
t1*
t2*
t3*
t4*
μ (MeV/G)
100
50
10
L*
2
3
4
5
6
Log10(PSD) (c/MeV/cm)^3
-4
-4.5
-5
-5.5
-6
-6.5
-7
-7.5
-8
-8.5
Dst (nT)
50
0
-50
-100
06/07
06/08
06/09
06/10
Time

Appendix Figure A1.

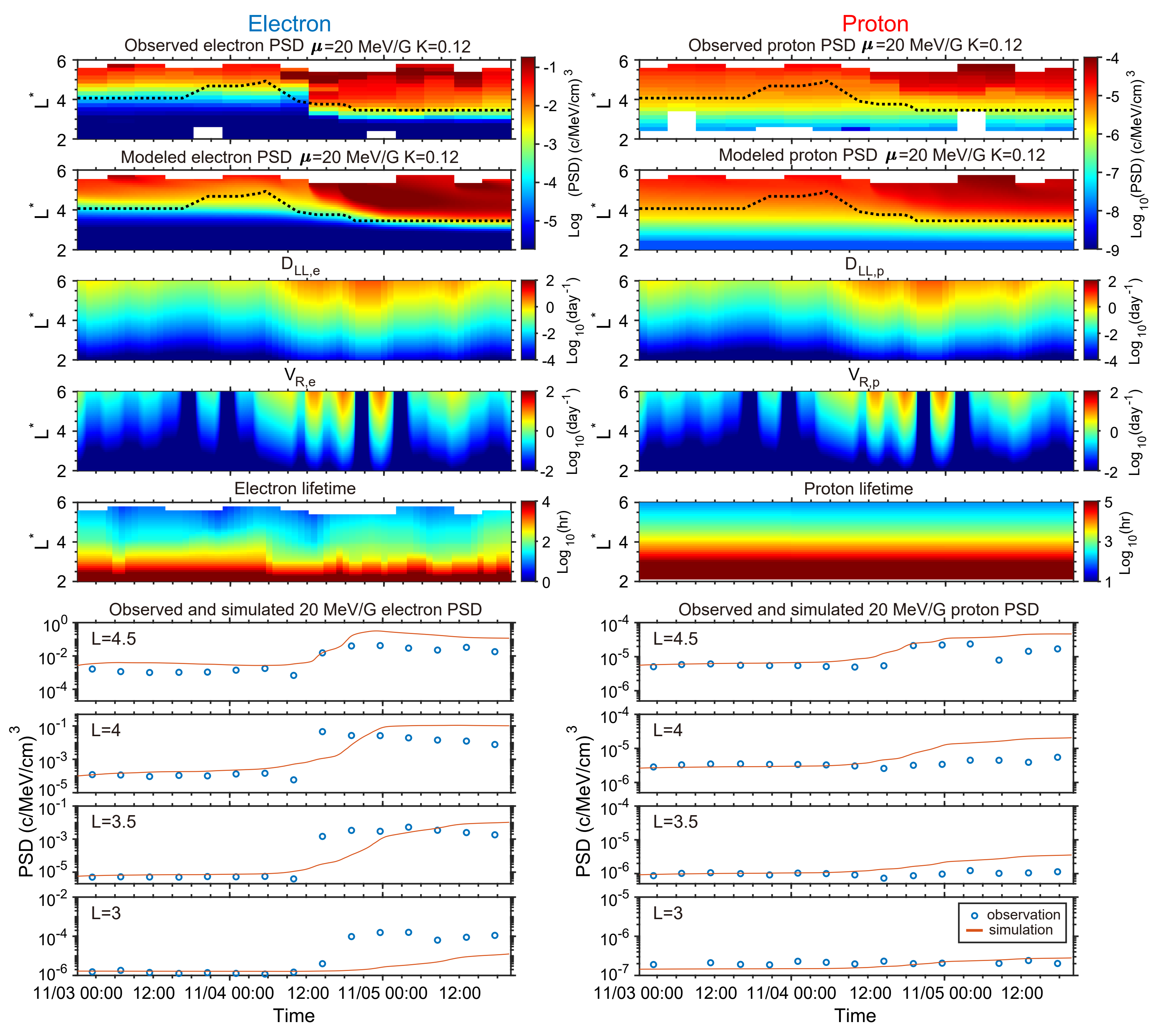

Electron
Proton
Observed electron PSD μ=20 MeV/G K=0.12
Modeled electron PSD μ=20 MeV/G K=0.12
Log (PSD) (c/MeV/cm)3
Observed proton PSD μ=20 MeV/G K=0.12
Modeled proton PSD μ=20 MeV/G K=0.12
Log10(PSD) (c/MeV/cm)3
DLL,e
DLL,p
Log10(day-1)
VR,e
VR,p
Electron lifetime
Proton lifetime
Log10(hr)
L*
Observed and simulated 20 MeV/G electron PSD
Observed and simulated 20 MeV/G proton PSD
L=4.5
L=4
L=3.5
L=3
PSD (c/MeV/cm)3
observation
simulation
11/03 00:00
12:00
11/04 00:00
12:00
11/05 00:00
12:00
Time

Appendix Figure A2.

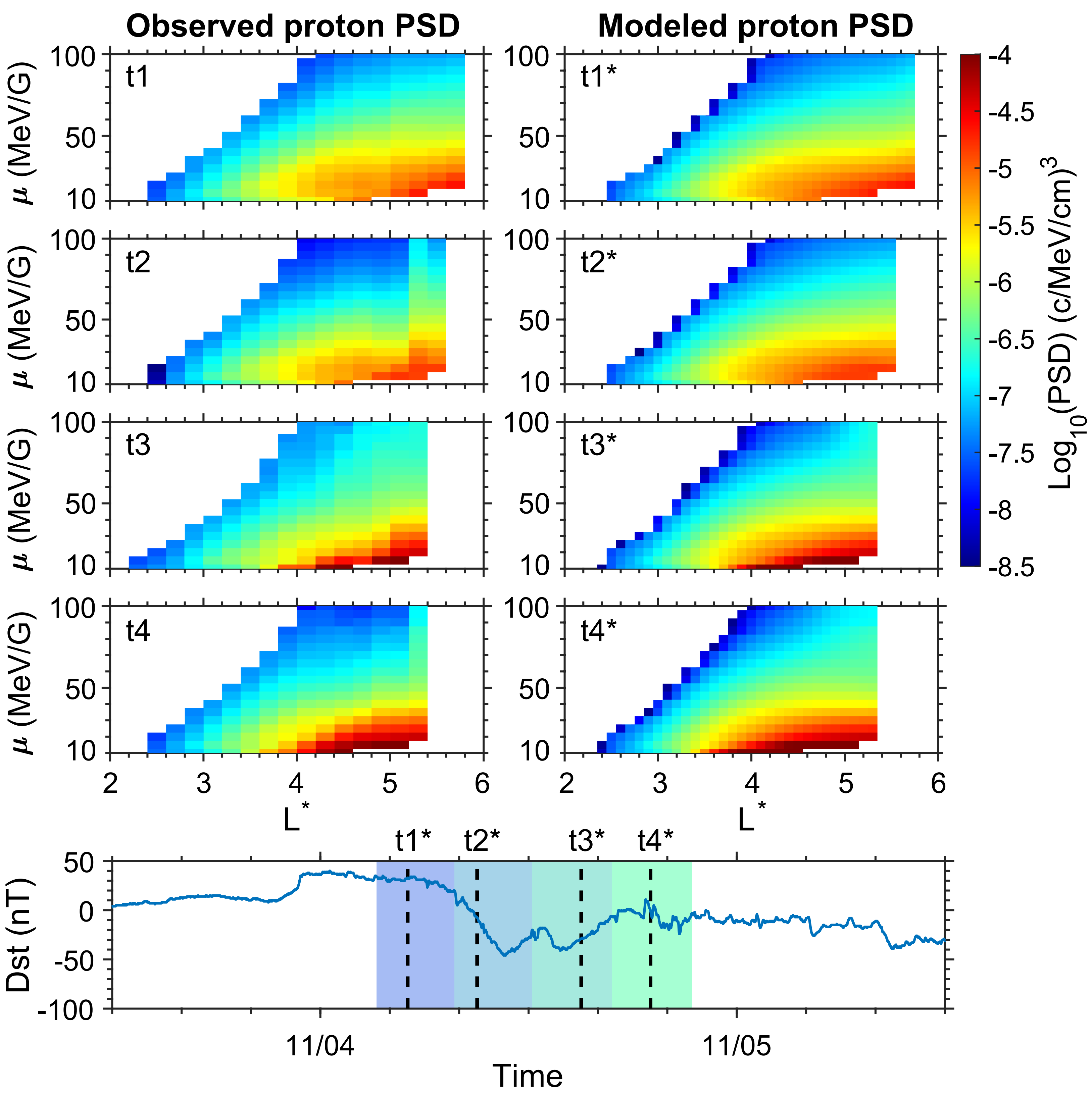
Observed proton PSD
Modeled proton PSD
t1
t2
t3
t4
t1*
t2*
t3*
t4*
μ (MeV/G)
100
50
10
2
3
4
5
6
L*
Log10(PSD) (c/MeV/cm)3
-4
-4.5
-5
-5.5
-6
-6.5
-7
-7.5
-8
-8.5
Dst (nT)
50
0
-50
-100
11/04
11/05
Time